Characteristics of ozone and particles in the near-surface atmosphere in urban area of the Yangtze River Delta, China

Huimin Chen[1], Bingliang Zhuang[1], Jane Liu[1,2], TijianWang[1], Shu Li[1], Min Xie[1], Mengmeng Li[1], Pulong Chen[1], Ming Zhao[1]

[1]School of Atmospheric Sciences, CMA-NJU Joint Laboratory for Climate Prediction Studies, Jiangsu Collaborative Innovation Center for Climate Change, Nanjing University, Nanjing 210023, China

[2]Department of Geography and Planning, University of Toronto, Toronto, M5S 3G3, Canada

Abstract

Aerosols and ozone have significant influences on air qualities, human health and climate changes. To further understand the characteristics and interactions among different urban air pollutants in the west Yangtze River Delta (YRD) region, continuous measurements of low layer atmospheric particles and trace gases have been performed at an urban site in Nanjing from September 2016 to February 2017 in this study. In urban area of west YRD, the mean PM_{10} and O_3 concentrations are 86.3 μg/m^3 and 37.7 ppb, respectively, with significant seasonal and diurnal variations. Particles, which are dominated by fine aerosols, are relatively scattering. And most of their optical properties have the similar variations to the aerosol concentrations. Results also show that west YRD could still suffer severe air pollutions, although the seasonal mean aerosol concentrations have been decreased in recent years. Even in cold seasons, O_3 could have about 40 days excess against to the National Ambient Air Quality Standards during the sampling period. Most of polluted episodes are

caused by local and sub-regional emissions. A case study for a typical O_3 and $PM_{2.5}$ episode in December 2016 demonstrates that the episode was generally associated with regional transport and stable weather system. Air pollutants were mostly transported from the western areas with high emissions, as well as with an anticyclone and high-pressure system in this region. Correlation analysis revels that the interaction between O_3 and PMs are complex with a combination of inhibition and promotion under different conditions. The inhibition effect might result from the reduction of photolysis frequency near surface due to aerosols besides their positive correlations with precursors, while the promotion effect is from the formation of secondary aerosols under high concentrations of oxidants and solar radiation. However, the interaction between O_3 and BC shows an inhibit effect due to its chemical stability. It is also indicated a VOC-sensitive regime for photochemical production of O_3 in this region. This study further improves the insight in the characteristics and interactions of main pollutants, and might have a certain contribution to improve the simulation and prediction of aerosols and gases in urban area of YRD.

1. Introduction

Particles, including black carbon (BC), $PM_{2.5}$, and PM_{10}, and trace gases, such as carbon monoxide (CO), ozone (O_3), nitric oxide and nitrogen dioxide (NO_x), and total reactive nitrogen (NO_y, which includes NO_x, aerosol nitrates (NO_3^-), nitric acid (HNO_3), N_2O_5, peroxyacetyl nitrate (PAN), and various nitrogen-containing organic compounds.), are important components in the troposphere because of their impacts on human health, biosphere and climate changes (e.g., Chameides et al., 1999a, b; Jerrett et al., 2009; Allen et al., 2012). Through long-range particle cycles, particles could interact with atmospheric trace gases from complex sources, especially ozone and its precursors, disturbing the earth's radiation budget (Sassen, 2002), or providing reactive surfaces for

heterogeneous reactions (Kumar et al., 2014), which leads to a great but hard problem for regional air quality (Zhang et al., 2008; van Donkelaar et al., 2010).

Over the decades, China is always one of the major source regions of particles, with BC and dust emission accounting for up to 25% of the global anthropogenic sources (Streets et al., 2001; Tegen and Schepanski, 2009). Relatively high levels of particle concentrations are mainly distributed in Beijin-Tianjin-Hebei area (BTH), Yangtze River Delta (YRD), and Pearl River Delta (PRD) regions (e.g., Zhang et al., 2008, 2012; Zhang et al., 2015), along with the rapid economic development. These regions consistently have the highest emissions of anthropogenic precursors (e.g., Wang et al., 2015; Wang et al., 2009b; Ding et al., 2013b; Zheng et al., 2010), which have led to severe region-wide air pollution. Earlier studies on particles mostly focused on concentrations estimation, the chemical characteristics, potential sources, as well as climate effects based on numerical simulations (e.g., Wu et al., 2012; Song et al., 2014; Xiao et al., 2012; Yu et al., 2015; Kristjánsson, 2002; Liao and Seinfeld, 2005; Zhuang et al., 2010, 2013, 2013b, 2018). However, a better understanding of spatial and temporal variations of particles can contribute to the adoption of effective measures to reduce air pollution, and real-time monitoring data is essential to better obtain the detailed variations (seasonal, monthly, and diurnal) on the city scale. In China, the research based on PMs observations, especially in the polluted regions above, have gradually expanded since 2012 due to the establishment of China's $PM_{2.5}$ air quality standards and gradual developments of nationwide PMs observation. The research is mainly related to the temporal and spatial distribution characteristics (e.g., Wang et al., 2015; Chen et al., 2016; Wu et al., 2012), and the effects of meteorological variables on aerosols (e.g., Zhang et al., 2015; Yan et al., 2016; Huang et al., 2015). In addition, many observations of BC have been made in the recent years, most of which concentrated on the analysis of the concentration level and the temporal and spatial variations (e.g., Verma et al., 2010; Wang et al., 2011b; Zhang et al., 2012). Some also revealed the correlations of carbonaceous aerosols (Pan et al., 2011; Zhuang et al., 2014b). Besides particles, because of the lack of nationwide O_3 monitoring data in earlier years, O_3 and its precursors (NO_x, NO_y, CO and VOCs etc.) pollution situations can only be discerned from limited campaign-type measurements in certain developed regions, for instance, Beijing in BTH area (Shao et al., 2006; Lin et al.,2008; Meng et al.,

2009), Guangzhou in PRD region (Zhang et al., 1998; Wang et al., 2003) and Lin'an in YRD region (Luo et al., 2000; Cheung and Wang 2001; Wang et al. 2001a, 2002, 2004; Guo et al. 2004b). Since 2005, the number of photochemical studies through observation data has increased in the PRD region in the south (Xue et al., 2014a), the BTH area in the north (Han, 2011), and the YRD region in the east (Shi et al., 2015). However, large gaps and uncertainties remain in the knowledge of characteristics of regional particles and O_3 pollution and its mitigation strategies due to the complexity of main sources, interaction between different aerosols, and changing meteorology filed.

The YRD is located in the eastern part of the Yangtze River Plain, adjacent to the most polluted North China Plain, including large cities of Shanghai, southern Jiangsu and northern Zhejiang. Taking up only 2 percent of the land area in China, this region produces over 20 percent of China's Gross Domestic Product (GDP). Nanjing, as the capital of Jiangsu Province, lies in the middle to west YRD. It covers an area over 6000 km^2, with more than 7.3 million residents (http://www.njtj.gov.cn/). Being the second largest commercial center after Shanghai in YRD, even the East China, Nanjing is highly urbanized and industrialized, especially the urban area. In addition, the complex monsoon and synoptic weather may play an important role in air pollution transport and formation in Nanjing. Therefore, the urban atmosphere in Nanjing is also heavily polluted by local emissions and long-distance transport of pollutants, which affects regional climate and air quality (Huang et al., 2013; Yi et al., 2015). Thus, the issue of air pollution in Nanjing deserves attentions. Previous studies using observation data in Nanjing often concentrated on characteristics of one of the particles (Deng et al., 2011; Shen et al., 2014; Zhuang et al., 2014) or ozone and its precursors (Tu et al., 2007; Wang et al., 2008; An et al., 2015), describing the temporal and spatial distributions, and the influence of meteorological effects, but lay less emphasis on the inter-species correlations and the combined effects of pollutants during severe pollution episodes. Ding et al. (2013b) described the characteristics of O_3 and $PM_{2.5}$ with near-surface observation data in rural Nanjing, but the detailed characteristics in urban Nanjing is not clear enough so far.

To fill the knowledge gap, continuous online measurements of particles, trace gases, and other relevant parameters were carried out at Gulou site in urban Nanjing about 80m above the ground,

an integrated measurement platform for the study of atmospheric environment and climate change. In this study, 6-month measurement of particles, trace gases, and other related variables at this site during September 2016~ February 2017 when air pollution occurred frequently is analyzed. Our work gives a synthetic analysis about their characteristics. The emphasis of our objective is to improve the insight in the characteristics, interactions of main pollutants, and the influence of integrated meteorology variables based on the observation data at an urban site above ground, and further investigate the possible underlying reasons and mechanisms. Firstly, an in-depth discussion on particles variations is performed, not limited to the concentrations but taking optical properties into consideration as well, to quantify the polluted level in detail. Secondly, a detailed description of O_3 variations can also be found in our study, including the analysis of the main precursors as trace gases (NO_x, NO_y and CO), to have a general and quantitative insight in O_3 pollution situations. Both of the pollutants are analyzed considering the effects of meteorology variables including but not limited to precipitation and temperature. Thirdly, analysis of inter-species correlations gives a relatively thorough overview of the interactions among various species, and deduction of the underlying chemical mechanisms based on the results of our study and previous studies is also presented in our study. Moreover, backward trajectories analysis is conducted for improving the knowledge of regional/sub-regional transport process in urban Nanjing. Finally, a case study for high particles and O_3 episode is implementing to emphasize the integrated influence of meteorological field on regional air pollution.

In the following, we describe the methodology in Section 2, which includes the measurement site and instruments. Results and discussions are presented in Section 3, consisting of overall temporal variation, correlation analysis, backward trajectory analysis, and case studies. A summary is given in Section 4.

2. Methodology

2.1 Brief Introduction to the Urban Atmospheric Observational Site

The Urban Atmospheric Observational Site is a regional atmospheric urban site located on the Gulou Campus of Nanjing University in the downtown area of Nanjing (32.05 °N,118.78 °E), and run by School of Atmospheric Sciences, Nanjing University. It is built on the roof of a 79.3m tall building, without any industrial pollution sources within a 30 km radius around but several main roads with evident traffic pollution, especially during rush hours. The sketch map of the site (not shown) and the corresponding climatology have been described in Zhu et al (2012).

The particles, O_3, NO_x, NO_y (including most oxides of nitrogen mentioned above with the exception of NH_3 and N_2O), CO, and wavelength-dependent aerosol optical parameters including aerosol scattering (σ_{ts}), back-scattering (σ_{bs}), and absorption (σ_a) coefficients have been routinely measured at the site during the time period from September 2016 to February 2017. The σ_a and concentrations of BC were derived from the measurements using a seven-channel Aethalometer (model AE-31, Magee Scientific, USA). The detailed calculation will be discussed below. The AE-31 model measures light attenuation (ATN) at seven wavelengths, including 370, 470, 520, 590, 660, 880 and 950 nm. The sample air is taken through a stainless-steel tube into the instruments, with a desired flow rate of 5.0 L min^{-1} and a sampling interval of 5 min during the whole period. The aerosol σ_{ts} and σ_{bs} were measured with a three-wavelength-integrating Nephelometer (Aurora 3000, Australia). Aurora 3000 measures aerosol light scattering, including σ_{ts} and σ_{bs} at 450, 525 and 635 nm, with a sampling interval of 1 min (Zhuang et al. 2017). The sample air was

taken through a 2m stainless-steel tube with a sampling interval of 1 min, top of which is 1.5m above the roof. The inlet has a rain cap and an external as well as an internal heater to prevent condensation. In cold seasons when RH in the tube was relatively low, maximum of which was lower than 75% and 80% of which was lower than 50% during sunny hours, therefore the internal heater was turned off. $PM_{2.5}$ and PM_{10} mass concentrations were measured using a mass analyzer (Thermo Instruments, THOM 1405-DF), which has been used to measure the mass concentration of $PM_{2.5}$, $PM_{2.5-10}$, and PM_{10} simultaneously. The hourly and daily mean mass concentrations are updated every 6 minutes, as well as the hourly base and reference mass concentrations. The sample air is taken through a stainless-steel tube into the instruments. Trace gases (CO, NO_x, NO_y and O_3) were measured every minute using online analyzers (Thermo Instruments, TEI 48i, 42i, 42iY, and 49i, respectively). Sample air was drawn from the 1.5m above the rooftop to the laboratory through a manifold connected to O_3, NO_x and CO analyzers with PFA Teflon tubes, while a separate sample line with a MoO converter was used for NO_y analyzer (Wang et al., 2002; Ding et al., 2013b) to convert other reactive nitrogen species including PAN, NO_3^- and HNO_3. Thus the measured quantity approximates total reactive nitrogen. Precision and instrument of all the measurements in this study are listed in Table 1.

Since aerosols are quite hygroscopic in China (e.g., Eichler et al., 2008; Liu et al., 2011; Ding et al., 2013b). All the instruments are installed in a laboratory with a constant temperature (24°C) and a low RH located on the building roof. Routine calibrations and maintenances were carried out for all these instruments during the sampling periods.

171 Monthly averaged meteorological parameters during the study period at the site are shown in Table
172 2. The air temperature at the site ranged from 6.64℃ in February to 24.88℃ in September. Both
173 higher relative humidity (RH) and more precipitation occurred in fall than winter, especially in
174 October. Visibility (Vis) varied in different months. The peak of the ultraviolet radiation (UV)
175 occurred in September, after which the radiation became weak till the end of January, and rose a
176 little afterwards.
177

178 **2.2 Calculation of the aerosol optical properties**

179 The wavelength-dependent σ_a, which is associated with the intensities of the incoming light and
180 remaining light after passing through a medium, can be calculated directly using the measured light
181 attenuations (ATN) through a quartz filter matrix, a percentage to represent the filter attenuation, as
182 well as BC mass concentrations (Petzold et al., 1997; Weingartner et al., 2003; Arnott et al., 2005;
183 Schmid et al., 2006).

184 $$\sigma_{a\,ATN,\ t(\lambda)} = \frac{(ATN_t(\lambda)\text{-}ATN_{t\text{-}1}(\lambda))}{\triangle t} \times \frac{A}{V}, \qquad (1)$$

185 where A (in m^2) is the area of the aerosol-laden filter spot, V is the volumetric sampling flow rate
186 (in L min^{-1}) and Δt is the time interval (=5 min) between t and t-1. $\sigma_{a\,\mathrm{ATN}}$, known as σ_a
187 without any correction, is larger than the actual aerosol absorption coefficient $\sigma_{a\,\mathrm{abs}}$ in general
188 because of (1). multiple-scattering of light at the filter fibers (multiple-scattering effect), and (2) the
189 instrumental response with increased particle loading on the filter (shadowing effect). The former
190 results in the overestimation of the σ_a, while the later causes underestimation of the σ_a. Thus, the
191 correction is needed and the calibration factors C and R (shown in Eq. 2) are introduced against the

192 scattering effect and shadowing effect, respectively:

193 $$\sigma_{a}^{\text{abs},\,t(\lambda)}=\frac{\sigma_{a}^{\text{ATN},\,t(\lambda)}}{C\times R}\ , \quad (2)$$

194 $$R_t(\lambda)=(\frac{1}{f}-1)\times\frac{\ln(ATN_t(\lambda))-\ln 10}{\ln 50-\ln 10}+1\ . \quad (3)$$

195

196 Previous investigation suggested that wavelength-dependent σ_a corrected by Schmid (Schmid et
197 al., 2006, SC2006 for short, hereinafter) might be the closest to the real ones in Nanjing (Collaud
198 Coen et al., 2010; Zhuang et al., 2015). Therefore, the SC2006 is adopted in this study. In this study,
199 the parameters in the correction procedure are derived from local optical properties (ω_0 and α_{ts}
200 were set to 0.922 and 1.51, respectively). The values of correction factors *C* and *R* are as follows:
201 *R*=1 when ATN≤10 and *f*=1.2, and *C* in Nanjing is 2.95, 3.37, 3.56, 3.79, 3.99, 4.51 and 4.64 at 370,
202 470, 520, 590, 660, 880 and 950 nm (Zhuang et al., 2015).

203

204 Measurement of Aurora 3000, a nephelometer with newly designed light sources based on light
205 emitting diodes, needs correction using Mie-theory for measurement artifacts. In this study,
206 correction was performed according to Müller et al. (2011). The raw total scattering coefficients
207 were corrected first by calculating first the Ångström exponents from the non-corrected scattering
208 coefficients and then following the formulas presented by Müller et al. (2011) where the tabulated
209 factors for no cutoff at the inlet were used. And based on corrected wavelength-dependent σ_a and
210 σ_{ts}, α_{ts} and α_a at 550 nm are estimated by the following:

211 $$\alpha_{a,470/660nm}=-\log(\sigma_{a,470nm}/\sigma_{a,660nm})/\log(470/660)\,, \quad (4)$$

212 $$\alpha_{ts,450/635nm}=-\log(\sigma_{ts,450nm}/\sigma_{ts,635nm})/\log(450/635)\,, \quad (5)$$

213

Meanwhile, aerosol asymmetry parameter (g), single-scattering albedo (ω_0) and extinction coefficient (σ_e) are further estimated:

$$\omega_0 = \frac{\sigma_{ts}}{\sigma_{ts}+\sigma_a}, \quad (6)$$

$$\sigma_e = \sigma_{ts} + \sigma_a, \quad (7)$$

2.3 HYSPLIT model

In order to understand the general transport characteristics of air masses recorded at this site, we conducted a 4 d (96 h) backward trajectory simulations during the cold seasons in 2016 using a Lagrangian dispersion model Hybrid Single-Particle Lagrangian Integrated Trajectory (HYSPLIT) (version 4.9) provided by the Air Resource Laboratory (ARL) of the USA National Oceanic and Atmospheric Administration (NOAA) (Draxler and Hess, 1998). HYSPLIT - 4 Model is capable of processing multiple gas input fields, multiple physical processes and different types of pollutant emission sources and has been widely used in the study of transport and diffusion of various pollutants in various regions (Mcgowan and Clark, 2008; Wang et al., 2011; Wang et al., 2015). It is one of the most extensively used atmospheric transport and dispersion models for the study of air parcel trajectories (Draxler and Rolph, 2013; Stein et al., 2016). In this study, backward trajectories were calculated and clustered using a stand-alone version of the GDAS (Ground Data Acquisition System) meteorological field (ftp://arlftp.arlhq.noaa.gov/pub/archives/gdas1). The GDAS data contain 6-hourly basic meteorological fields on pressure surfaces, with the spatial resolution of 1.0°, corresponding to the 00, 06, 12, 18 UTC, respectively. In this study, the data are also converted to hemispheric 144 by 73 polar stereographic grids, which is the same grid configuration as the dataset

applied in synoptic weather classification. For each synoptic weather pattern, the backward trajectories were started at Gulou site in Nanjing (32°N, 118.8°E).

3. Results and discussion

3.1 Characteristics of particulate matter in Nanjing

The hourly-mean concentrations and optical properties of particles at Gulou site during the cold seasons in 2016 are shown in Fig 1. Gaps in the time series are missing values. Observations show that peaks and valleys of BC, $PM_{2.5}$ and PM_{10} occur simultaneously in general (Fig 1a), probably because the three particles originate mostly from the same sources, i.e., fossil fuel burning and traffic activities. It has also been addressed in previous work (e.g., Wang et al., 2008; Chow et al., 2011; Schleicher et al., 2013; Zhuang et al., 2014b; Gong et al., 2015).

BC concentration ranged from 0.064 to 15.609 μg/m³. Seasonal mean of BC concentration was 2.126 μg/m³ in SON and 3.083 μg/m³ in DJF, with a standard deviation of 1.457 and 1.827 μg/m³, respectively. It was low in September and October, usually below 6 μg/m³, but higher in other months. Although BC concentration was relatively low, it was extremely high in particular periods, , such as in mid-November, early and late December, early January, and mid-to-late February, suggesting occurrences of substantial BC pollution events. $PM_{2.5}$ and PM_{10} concentration ranged from 0.8 to 256.4 μg/m³ and from 1.1 to 343.4 μg/m³, respectively. Seasonal mean of $PM_{2.5}$ concentration was 43.1 μg/m³ in SON and 73.2 μg/m³ in DJF, with a standard deviation of 25.4 and 40.0 μg/m³, respectively. PM_{10} averaged 67.6 μg/m³ in SON and 105.0 μg/m³ in DJF, with a standard deviation of 39.1 and 54.0 μg/m³, respectively. $PM_{2.5}$ and PM_{10} concentration were generally below

120 and 200 μg/m³, respectively. Remarkable increases existed especially when BC concentration was high. Additionally, the high concentrations of PMs in early October possibly resulted from the increase in scattering aerosols, since absorption coefficient and BC, one of typical absorbing aerosols, did not show such peak, while scatter coefficient experienced a sharp increase during that period. It is found that both BC and PMs levels in Nanjing became lower compared to those in earlier years, which is possibly due to the strengthening energy conservation and reduction of pollution emissions from 2014. For instance, seasonal average in SON and DJF were reported 4339 and 4189 ng/m^3 in urban Nanjing during 2012 in Zhuang et al. (2014b), and Ding et al. (2013b) stated a 1-year average about 75 μg/m^3 of $PM_{2.5}$ in rural area of Nanjing form August 2011 to July 2012, while Wang et al. (2014) suggested that annual average of $PM_{2.5}$ and PM_{10} were 75 and 135 μg/m^3 in Nanjing during 2013, respectively.

Monthly variations of particles in the cold seasons in 2016 were distinguished (Fig.2). The concentrations increased from October to December and decreased a little afterwards but remained relatively high in January and February. The lowest monthly concentrations of BC, $PM_{2.5}$, and PM_{10} occurred in October, being 1.8, 39.2, and 59.8 μg/m³, respectively, while the highest monthly concentrations occurred in December, being 3.7, 85.0, and 123.1 μg/m³, respectively, which were about twice of those in October. Monthly variations of BC were different from those in previous studies in YRD. For instance, Pan et al. (2011) pointed out an extremely high concentration in October in Mt. Huang, which was attributed to combustion of biomasses as well as the dynamic transport and stable planetary boundary layer (PBL) stratification in the transitional periods of the winter monsoon (October). For PMs, monthly behavior was basically similar to what has been

reported in previous studies in YRD, increasing from September to December in general (Chen et al., 2016), except the decrease in October. Generally, two key factors could impact particle concentrations: meteorology and emissions. Heavy precipitation in October when average rainfall was 3.1 mm, and the frequency of daily rainfall exceeding 50mm was over 30% (Table.2), had a strong scavenging effect, which might directly lead to low levels of particles despite the influence of biomass burning addressed in Pan et al. (2011). Anthropogenic particle emissions from fossil fuel over China increased after summer and showed a sharp increase from November to January (Zhang et al., 2009), and emission rates in southwest (Sichuan basin), central to north, and northeast China, as well as YRD and PRD were higher in winter (Zhuang et al., 2018), especially in residential, industry and power emissions (Li et al., 2017). And during the autumn harvest (September~ November), though not so much as that in summer, the crop burning emissions in still make contribution to pollutants (Yang et al., 2008). Yin et al. (2016) discussed the spatial distribution of crop residue burning from September to December in 2015, suggesting autumn crop residue burning in surrounding regions like Shandong, Anhui and Henan Provinces, thus, particles in Nanjing might also be subject to these large-scale burning of crop residues (Qian et al., 2014). According to Huang et al. (2012) and Li et al. (2016), spatiotemporal distribution of agricultural fire occurrences in China during 2003~ 2010 as well as 2012 has been presented associated with the spatial distribution of CO emission from residue open burning. Both of them suggested the crop residue burning in autumn is noteworthy and Jiangsu as well as the surrounding provinces are the regions with highest emissions. Besides, sub-regional transport also plays an important role, for example, in winter, air masses coming from North China Plain, which accounts for 31%, have high particles concentrations (Sect 3.4).

Substantial diurnal cycles of the particles are also observed (Fig.3). Particles levels were high during 7:00~9:00 and 22:00~0:00 LT but low in afternoon (13:00~15:00 LT). High concentrations during 7~9 am might be caused by the vehicle emissions (as mentioned in Section 2, several main roads with apparent traffic pollution surround the site). A higher vehicle volume showed during 17:00~ 20:00 LT in Nanjing, while the high concentrations occurred during 22:00~ 0:00 LT. A lower temperature and a more stable atmosphere stratification after sunset (17:00~18:00 LT) often lead to frequent temperature inversion and low height of planetary boundary layer (Jiang et al., 2014), which is not conductive to the diffusion of pollutants, and the concentrations of particles accumulate and remain high from the evening to early morning. For low levels in afternoon, it is mainly induced by well-developed boundary layer. Because the atmosphere become less stable with the increasing temperature, and strong turbulent exchange as well as vertical diffusion are favorable to the diffusion of pollutants, particles concentrations decrease to a minimum in the afternoon. Similar phenomenon of PMs has been observed in previous studies in Nanjing (Chen et al., 2016; Ding et al., 2013b), while a different pattern is discussed in Pan et al. (2011) in Mt. Huang, a rural site in YRD, due to different emission sources (less vehicle emission) and meteorology effects (effect of valley breezing). Fig. 3 also shows that the peak values of fine particle concentrations often occur one or two hours later than those of BC concentrations, with high values at around 10 am and low values at around 5 pm. According to Roberts and Friedlander (1976) and Khoder (2002), atmospheric photochemical reactions are extremely active under conditions of strong radiation and high temperature especially during daytime, thus, more secondary aerosol particles (like sulfate particles) are likely to generate, and the concentrations of fine particles in the atmosphere will

increase.

3.2 Characteristics of trace gases in Nanjing

Fig.4 shows hourly-mean concentrations of trace gases at Gulou site during the cold seasons in 2016. In general, as main precursors of O_3, NO_x, NO_y, and CO generally show different pattern with O_3, such as when the precursors levels remained high from November to January, O_3 levels were relatively low (Xie et al., 2016; Wang et al., 2017). Also, the precursors concentrations varied greatly, especially in DJF (with several peaks), possibly because of the frequent shifting of air masses from the clean interior continent and heavily polluted urban plumes in the heating period (normally from November to March in Northern China) (Pan et al., 2011).

Concentrations of trace gases, including CO (176~ 2852 ppb), NO_x (2.7~ 80.0 ppb), NO_y (3.6~ 158.4 ppb), and O_3 (0.2~ 235.7 ppb), varied a lot in the study period. Seasonal mean of O_3 was 42.3 ppb in SON and 33.1 ppb in DJF, with a standard deviation of 40.1 and 24.4 ppb, respectively. As shown in Fig.4, O_3 concentration was extremely high during the entire September in 2016, with a maximum over 200 ppb, and decreased sharply after mid-October, basically keeping a low level below 100 ppb, until early February when it began to increase. Seasonal averages of NO_x and NO_y, were 21.4 and 28.6ppb in SON, with a deviation of 20.5, and 40.1 ppb, respectively. In DJF, mean concentrations of NO_x and NO_y were 27.6 and 37.0 ppb, with a deviation of 15.5 and 23.1 ppb. And seasonal averages of CO were 753 ppb in SON, and 950 ppb in DJF, with a deviation of 353 and 388 ppb, respectively. The precursors concentrations were high from November to mid-January,

and low in September. Moreover, it is suggested that O_3 concentration is higher compared to the results in previous studies based on the measurement at ground sites in Nanjing (Xie et al., 2016; An et al., 2015; Ding et al., 2013b), implying a more pressing environmental issue of near-surface O_3 problem in urban area.

Monthly variations of trace gases are shown in Fig.5. It is noticeable that the different patterns occur in O_3 and its precursors. Observations show that O_3 concentration decreased after the lasting extremely high level in September until November and increased a little afterwards. Highest concentration of O_3 was found in September and lowest in November, being 74.8 and 23.4 ppb, respectively. This pattern might be attributed to the solar radiation and emissions. For instance, in September when solar radiation was strong (maximum UV over 55 W/m^2), it would contribute greatly to O_3 formation, and precursors were at relatively high levels (CO, NO_x, and NO_y were about 600, 15 and 20 ppb, respectively), though not as high as those in cold days. CO, NO_x and NO_y peaked in December correspondingly at 1064, 31.8 and 41.7 ppb. The precursors reached the lowest level in September, being 620, 14.5, and 20.8 ppb, respectively. In addition, the pattern of precursors is analogous to those in previous studies (Xie et al., 2016; Ding et al., 2013b), but with a relatively lower concentration, especially NO_x and NO_y, which might also result from the large-scale reduction of pollution emissions.

Fig. 6 (a) shows the diurnal variations of the trace gases (O_3, NO_x, NO_y, and CO). The concentration of O_3 is the lowest around 7:00 LT and rises rapidly until reaching the peak in the middle of the day at 15:00 LT. It keeps decreasing sharply after the afternoon peak till sunset. During the nighttime,

365 the concentration of O_3 decreases slowly and remains low. With respect to NO_x and NO_y, peak
366 appears at around 9:00 LT, with another high value occurring at night (21:00~ 0:00 LT), both of
367 which coincide with the rush hours in the city, when large amounts of vehicle emissions are released.
368 The morning peak is slightly higher than the night one in general. Besides emissions, these diurnal
369 variation patterns of O_3 and NO_x (NO_y) mainly result from the photochemical processes and the
370 meteorological conditions. Simultaneous measurement of O_3 and UV shows that the O_3
371 concentration is highly correlated to UV (R=0.47). The ultraviolet radiation (UV) at Gulou started
372 to increase at about 7:00 LT (Fig.6 (b)), which could induce a series of photochemical reactions
373 including the formation of peroxy radicals (HO_2 and RO_2 etc.) and the photolysis of NO_2. From
374 8:00 to 15:00 LT, the increase in UV enhances the O_3 formation by promoting the production of
375 NO_2 and OH from NO and peroxy radicals. The diurnal range of O_3 concentration (the difference
376 between the maximum at 15:00 LT and the minimum at 7:00 LT) is relatively high (45.1 ppb),
377 suggesting the active chemical reactions as well. It is also noticeable that the O_3 peaks 2 hours after
378 the UV maximum, suggesting the time to take for the chemical reactions. The slightly reduction of
379 O_3 and NO_x in the early morning (3:00~7:00 LT) is likely due to NO_x titration. The development of
380 the planetary boundary layer (PBL) can also modulate pollutant concentrations. The concentration
381 of a pollutant is diluted when PBL rises during the daytime and enhanced in the low nocturnal PBL
382 that favors pollutant accumulation, after comparing Fig.6 (a) with the reported diurnal variation of
383 PBL height in Nanjing (Jiang et al., 2014; Xie et al., 2016). And that is also the reason for the
384 difference of peak time between the emission rate and NO_x (NO_y) concentration, which is similar
385 to particles to some degree. The abovementioned diurnal cycles in O_3 and NO_x (NO_y) concentration
386 follow the typical patterns at other sites in Nanjing (Tu et al., 2007; Ding et al., 2013b; Xie et al,

2016). The daily variation of CO concentration is found to be similar to that of BC, such as morning peak during rush hours, afternoon dip at around 15:00 LT, and accumulation at night. A remarkable correlation has been found in a number of previous studies (e.g., Jennings et al., 1996; Derwent et al., 2001; Badarinath et al., 2007; Spackman et al., 2008; Pan et al., 2011; Zhuang et al., 2014b). Besides, BC is mostly produced by the incomplete combustion of carbonaceous material, and so is carbon monoxide (CO) (Pan et al., 2011), thus, both BC and CO might come from the same sources, mostly from combustions of domestic bio-fuel, industry-coal, and vehicle-gasoline (Zhuang et al., 2014b). The effect of meteorology, i.e., the development of PBL, influences the diurnal pattern as mentioned in Section 3.1, especially the afternoon dip and night accumulation. Moreover, as one of main precursors of O_3, increase in O_3 levels in the afternoon might also contribute to the lowest concentration at 15:00 LT.

Table 5 further provides the statistics of O_3, $PM_{2.5}$ and PM_{10} mass concentrations with a comparison to the National Ambient Air Quality Standards in China (NAAQS-CN) released in 2012 by the China State Council and will be implemented nationwide in 2016 (MEP, 2012). According to NAAQS-CN for $PM_{2.5}$ and PM_{10} (75 $\mu g/m^3$ of $PM_{2.5}$ and 150 $\mu g/m^3$ of PM_{10} for 24h average concentration), there were 48 days of $PM_{2.5}$ exceedances, accounting for about 30% during the study period, and 14 days of PM_{10} exceedances, lower than the $PM_{2.5}$ exceedances. Days of PMs exceedances mainly occurred during DJF. The days of exceedances decreased. Ding et al. (2013b) reported 99 days of $PM_{2.5}$ exceedances in total from September 2011 to February 2012, and Wang et al. (2014) suggested that non-attainment rates in Nanjing from September 2013 to February 2014 were over 40% and 70% in SON and DJF, respectively. These results suggest that particles control

409 policies are well-implemented in Nanjing although particles remain a severe pollution problem in
410 the YRD region. According to NAAQS-CN for O_3 (160 μg/m^3 for 8 h average and 200 μg/m^3 for 1
411 h average), 37 days of exceedances occurred (Table 5), covering 20% of the period and mostly in
412 September and February when the air temperature was relatively high. In contrast to particulate
413 matter, days of O_3 exceedances increases greatly. Wang et al. (2014) reported a 11.4% contribution
414 of O_3 as the major pollutant on non-attainment days in cold seasons in 2013 in south-east China,
415 and Tu et al. (2007) reported frequency of days with O_3 exceedance for cold seasons in 2000~2002
416 in urban Nanjing was 6.3%. O_3 levels in the rural areas are generally higher than those in the city
417 centers (Zhang et al., 2008; Geng et al., 2008; Xie et al., 2016). Thus, high O_3 concentration and
418 severe air pollution at Gulou, an urban site, probably imply a severer O_3 pollution problem in the
419 entire YRD region. Moreover, note that this study only discusses the O_3 concentration in the cold
420 seasons when it is relatively low, and it might suggest a severer problem in warm seasons.
421

422 **3.3 Inter-species correlations**

423 Correlations between different species have been analyzed to help interpret the data and gain
424 insights into the underlying mechanisms/processes. Because precipitation could impact wet
425 scavenging processes for particles and other aerosols (Table 6), the data in rainy condition has been
426 eliminated.
427

428 The scatter plot of O_3 and NO_x measured at the site color-coded with air temperature is given in
429 Fig.7 (a). As discussed in previous studies (Xie et al., 2016; Ding et al., 2013b), measured O_3

presents an overall negative correlation with NO_x. The negative correlation mainly exists for data of relatively low air temperature, suggesting a titration effect of freshly emitted NO_x with O_3, especially at nighttime. However, the slope gets less rigid when air temperature rises, and tend to be positive with a high temperature (over 25℃) and low level of NO_x (below 30 ppb). These results possibly suggest a strong photochemical production of O_3 in this region under high temperature with strong radiation like in September, leading to the seasonal cycle pattern of O_3 shown in Fig. 5 (a).

Fig.7 (b) provides a scatter plot of $PM_{2.5}$ and visibility (Vis) color-coded with relative humidity (RH). For a better understanding of the relationship between the variables, we have performed a linear fit of the visibility with the $PM_{2.5}$ concentration when RH ≤ 70%, 70% <RH ≤ 80%, and 80% < RH ≤ 90%, to find out the relationship among these factors, and the fitting curves are $[PM_{2.5}] = 366.72[Vis]^{-0.745}$ ($R^2 = 0.7196$), $[PM_{2.5}] = 337.16[Vis]^{-0.855}$ ($R^2 = 0.8692$), and $[PM_{2.5}] = 248.6[Vis]^{-0.852}$ ($R^2 = 0.8279$), respectively. It is found that visibility decreases with the concentration of $PM_{2.5}$ in a power function with a negative exponent, and the inverse relationship between visibility and aerosols concentrations as well as relative humidity has also been discussed in previous studies based on the observations in YRD (e.g., Deng et al., 2011; Xiao et al., 2011; Jiang et al., 2018). The correlation is stronger than that in Lin'an, a rural site not far from Nanjing (Jiang et al., 2018). The concentrations of particles would increase the extinction coefficient, while the visibility (Vis) is related to the coefficients through:

$$Vis = \frac{3.91}{\sigma_e} \quad (8)$$

where Vis is the visibility and σ_e is the extinction coefficient (Larson et.al, 1989). As for the effect of relative humidity (RH) on the visibility, according to Mie theory, with the increase of the relative humidity, the radius of the wet particle also increases, and so the extinction coefficient, which leads to the decrease in visibility.

According to the scatter plots of $PM_{2.5}$–O_3 and BC–O_3 color-coded with air temperature (Fig.8), $PM_{2.5}$ and BC are negatively correlated with O_3 in general. It is also noticeable that a negative correlation between $PM_{2.5}$ and O_3 could be found for low air temperature samples while a positive correlation exists for those under a high temperature. Similar results were also found at a rural site in Nanjing (Ding et al., 2013b). Besides, BC is in a negative correlation with O_3 under low air temperature, but tend less-correlated with O_3 when the temperature rises. $PM_{2.5}$ is well-correlated with O_3 precursors, such as NO_x (Fig.10 (b)) and CO. Therefore, the anti-correlation in Fig.8 (a) for cold air is likely due to the titration effect of high NO concentrations associated with high primary $PM_{2.5}$ levels. Additionally, the increasing slope under high air temperature might be related to the formation of secondary fine particles, especially the high conversion rate of SO_2 to sulfate under the effect of the high concentration of oxidants (O_3) and solar radiation (Roberts and Friedlander, 1976; Khoder, 2002). Previous studies of $PM_{2.5}$ chemical compositions in Shanghai (Wang et al., 2006) and Nanjing (Ding et al., 2013b) suggested that sulfate was the most dominate ion in $PM_{2.5}$. Ding et al. (2013b) also suggested formation of secondary organic aerosols with high O_3 concentration could lead to the positive correlation because biogenic emission of VOCs is high under a condition of high air temperature and solar radiation in summer. However, the study is performed during cold seasons when air temperature is relatively lower and the biogenic emission of VOCs are likely lower, so the

positive correlation is less pronounced. As for BC, it also shows a good correlation with NO_x (Fig.10 (c)) and CO, which contributes to the inverse correlation for cold air. Since BC is insoluble in polar and non-polar solvents and still remains stable when air or oxygen is heated to 350 ~ 400°C, it's hard to be generated or cleared through chemical reactions. And that is probably the reason why the correlation between BC and O_3 is obscurer compared to the one between $PM_{2.5}$ and O_3 when air temperature rises. Moreover, as shown in Fig.9, O_3 is well correlated with UV (daily mean values are used due to the remarkable diurnal variation), suggesting the significant role UV plays in O3 production, while $PM_{2.5}$ is generally negatively correlated with UV. Previous findings based on various numerical models also suggest that particles can affect actinic flux of UV radiation, and inhibit the photolysis reactions near surface in reducing the photolysis frequencies in the atmosphere, like the frequency of $O_3 \rightarrow O(^1D)$ (e.g., Li et al., 2005; Deng et al., 2010; Li et al., 2011; Li et al., 2018). In central Nanjing, as implied in Li et al. (2017), high concentrations of aerosols could result in a 0.1−5.0 ppb (12.0%) reduction of near-surface ozone. Thus, they might result in the decrease of O_3 concentration near the ground to some degree. However, the detailed mechanisms still need to be further investigated by long-term measurement of aerosol chemical composition combined with numerical models.

Scatter plots of CO–NO_x, $PM_{2.5}$–NO_x, and BC–NO_x, are given in Figs. 10 (a)~ (c), with data points color-coded with the concentration of O_3. Fig.10 (b) and (c) show a good positive correlation between $PM_{2.5}$ and NO_x, as well as BC and NO_x as mentioned above, suggesting that the particles at the site are mainly associated with similar sources like combustion and traffic activities (Wang et al., 2006; Ding et al., 2013b; Zhuang et al., 2014b). It is found that high O_3 levels are generally

related to air masses of high CO/NO_x or particles/NO_x ratio. An increase in CO, as well as $PM_{2.5}$ and BC, always results in higher O_3 concentration for NO_x lower than 40 ppb, while NO_x reverses. To be specific, when NO_x reduces for CO lower than 1500 ppb, O_3 has a sharp increase, and an increase in the CO level would lead to an in increase in the O_3 concentration, especially when NO_x is lower than 40 ppb. The concentration of O_3 is sensitive to the level of its precursors, and the O_3 formation regime often includes NO_x-sensitive O_3 formation regime and VOCs-sensitive O_3 formation regime. If O_3 formation is under VOC-sensitive regime, a reduction in the NO_x concentration will lead to an increase in the O_3 concentration, which is used to determine the O_3 photochemical production in the region is VOC-limited or NOx-limited based on observation data (Geng et al., 2008; Ding et al., 2013b). In our study, we have no VOCs measurement, thus CO is chosen as the reference tracer, because mixing ratios of CO showed significant correlations with the measured levels of most anthropogenic VOCs, which has been verified in many previous studies (e.g., Baker et al., 2008; von Schneidemesser et al., 2010; Wang et al., 2014). In addition, as a significant precursor of O_3, CO also plays a similar role as VOCs. HO_2 produced from the oxidation reaction of CO with OH radicals could initiate photochemical reactions which result in the net formation of O_3 (Novelli et al., 1998; Atkinson et al., 2000; Gao et al., 2005). Thus, the CO–O_3–NO_x relationship may reflect the correlation of VOCs, NO_x, and O_3 in this region to some degree. Therefore, we suggest that the region is VOC-sensitive. Geng et al. (2008) reported a VOC-sensitive regime in urban Shanghai combining the measured and modeling results, and Ding et al. (2013b) also reported a VOC-sensitive regime in rural area in Nanjing using the observation data. And the $PM_{2.5}$-O_3-NO_x and BC-O_3-NO_x relationship show the similar pattern, possibly because they are well-correlated with CO.

517

518 **3.4 Backward Trajectory Analysis**

519 The cluster means of the backward trajectory at 100 m from Gulou, Nanjing, in 2016 fall (Fig.11)
520 and winter (Fig. 13) suggest different air flows transported to Nanjing from long distances. In
521 general, the aerosol kinds and optical properties are characterized differently with different air
522 masses in the two seasons, which are further analyzed by their origins in SON and DJF (Figs.12 and
523 14). Figs. 12 and 14 show the main concentrations of particles and trace gases, the ratio of $PM_{2.5}$ to
524 PM_{10}, as well as the values of the aerosol optical properties of different clusters during SON and
525 DJF, respectively. Because PM_{10} varies similarly to $PM_{2.5}$, while NO_x varies analogously to NO_y,
526 we only present the variations of $PM_{2.5}$ and NO_y with cluster here. Also, because σ_a, σ_{ts} and σ_{bs}
527 have good correlations with particle concentrations (Zhuang et al., 2014a) and g is greatly affected
528 by relative humidity, we discuss the variation of α_{ts} and ω_0 with cluster here.

529

530 In SON, the dominant air masses are from the East China Sea passing through urban agglomeration
531 regions (cluster 3), and less-developed regions (cluster 2) of the YRD, and from northern continent
532 away from Nanjing passing through oceans and urban agglomeration regions (cluster 4). It is found
533 that although air masses in cluster 3, cluster 4 and cluster 2 all pass through the oceans and have the
534 same level of RH, differences still exist among the clusters. The air masses have to cross the urban
535 agglomeration (from Shanghai to Nanjing) of YRD when they arrive in Nanjing in cluster 3 but pass
536 less-developed regions (north Jiangsu Province) in cluster 4 and cluster 2. In YRD, emissions of
537 aerosols and trace gases are much stronger in urban agglomeration regions (Zhang et al., 2009;

538 Zhuang et al., 2013). It is also noticeable that concentrations of aerosols in cluster 4 are mostly
539 lower, which may result from its avoidance from BTH regions, also a megacities and urban
540 agglomeration. In addition, air masses from the west of cluster 1 contain the highest concentrations
541 of PMs and precursors., Air masses pass central China with high emissions of particles and trace
542 gases according to MERRA data (https://gmao.gsfc.nasa.gov/reanalysis/MERRA) and Zhuang et
543 al. (2015). Also, high concentrations of these aerosols are also reflected in a high aerosol optical
544 depth (AOD) according to the MISR data (https://giovanni.gsfc.nasa.gov/giovanni). The ratio of
545 $PM_{2.5}$ to PM_{10} represents the number of particles deriving from secondary pollution progress
546 compared to those from primary pollution progress to some extent. In SON, ratios of clusters 1~3
547 are relatively close (all over 60%) with a maximum of cluster 3, which means particles generating
548 from secondary pollution progress in the 3 clusters have a similar rate. O_3 concentrations among the
549 4 clusters are different. Despite negative correlations of O_3 with its precursors and particles, the
550 concentration of O_3 in cluster 3 is higher than that in cluster 4, possibly because radiation in cluster
551 3 is stronger. The size of the aerosols in cluster 1 are finest (α_{ts} is the largest in Fig. 12g), because
552 the other 3 clusters all pass through oceans before arriving Nanjing with higher relative humidity.
553 Therefore, it is likely to enhance particles hygroscopicity. ω_0 is also the largest in cluster 1, and it
554 suggests that aerosols in cluster 1 are the most scattering, corresponding with the highest
555 concentration of $PM_{2.5}$.
556
557 In DJF, air masses come from the local region (cluster 2), north-west areas (cluster 1), and northern
558 regions far from Nanjing (cluster 4). Air masses from cluster 1 and cluster 2 both account for over
559 30% of the total aerosol characteristics and are more polluted with relatively high levels of particles,

CO, and NO_x. Air masses in cluster 1 come from Shandong Province while those in cluster 2 come from local areas. Particles and trace gases concentrations of cluster 2 are higher than those of cluster 1 to some extent, implying the severer air pollution problem in YRD region. The concentration of O_3, similar to that in SON, is affected by radiation besides precursors levels. Thus, O_3 concentration in cluster 2 is a little higher than that in cluster 1. The ratios of $PM_{2.5}$ to PM_{10} of cluster 1 and cluster 2 are approximately equal, over 70%. The size of aerosols in cluster 1 and 2 are coarser, however, probably due to the higher RH (over 65%). Aerosols in cluster 1 are more scattering compared to those in cluster 2. The trajectories of cluster 3 and cluster 4 are analogous to those in SON, respectively, but more polluted, probably due to more emissions in DJF especially in north China and weaker flow from ocean in DJF.

3.5 Case Study

For further understanding of the causes for high pollutants episodes, especially high particles and O_3 episodes, detailed analysis of a typical episode from 2016 December 3-6 is presented in this section.

Fig.15 (a) and (b) show that high O_3 concentration (over 80 ppb) occurred on December 4 with broad O_3 peaks (over 60 ppb) in the following days, while the average O_3 during the cold seasons was 37.7 ppb. Though there is a lack of PMs concentrations because of the instrument breakdown, high concentrations of PMs might possibly occur referring to the relatively high σ_e (over 500 Mm^{-1}) and BC concentration (over 6 $\mu g/m^3$) on December 4th. Both PMs reach a maximum on

December 5th ($PM_{2.5}$ over 200 μg/m^3 and PM_{10} over 300 μg/m^3), over 3 times of the averages. Besides, NO_x, NO_y, have reached high levels since December 4th (NO_x over 70 ppb and NO_y over 100 ppb). It is also noticeable that ω_0 has a relatively sharp decrease from December 4, especially on December 5 when particle concentrations were extremely high, probably suggesting that the ratio of PM_{10} became higher. Meanwhile, a relatively sharp increase occurred in α_{ts}, without any obvious variation in α_a, though, implying that scattering aerosols could take the leading role during this episode. It is also found that this case occurred under calm conditions before the passage of a cold front, which was at the front of a continental high-pressure system originating from Mongolia and sweeping over Nanjing (Fig.15 (c)), and the decrease in temperature with high-pressure system dominating eastern China were also detected on December 6. Backward trajectory analysis for the past 96 hours (Fig.15 (d)) were conducted from December 5 at 8 pm, including the maximum of O_3 on December 4 and PMs on December 5. It is suggested that predominant wind was just in time from the NW directions. Therefore, air masses with high particles and O_3 concentrations would be transported to Nanjing. It was also clearly detected in Nanjing during these days, such as the relatively high O_3 during nighttime on December 5 and 6. The highest O_3 on December 4 together with high particles and primary pollutants NO_x and NO_y suggests a strong in situ photochemical production in mixed regional plumes under the influence of high-pressure system. Previous studies (Luo et al., 2000; Wang et al., 2006; Ding et al., 2013b) reported that the anticyclonic conditions, e.g.,, sunny weather and low wind velocities, are favorable for pollution accumulation and O_3 production. Results in this case clearly demonstrate sub-regional transport of primary and secondary air pollutants within the YRD region under such weather system.

4. Conclusion

In this study, particles (BC and PMs) and trace gases (O_3 and related precursors) in polluted seasons, are investigated based on continuous measurements of concentrations and optical properties in the urban area of Nanjing. The characteristics and underlying reasons are comprehensively discussed from perspectives of temporal variations, inter-species correlations, trajectories analysis, and case studies associated with weather data and Lagrangian dispersion modeling.

Measurements show that average concentrations of PM_{10} was 86.3 μg/m^3, with BC and $PM_{2.5}$ accounting for 3% and 67%, respectively. 48 and 14 days of $PM_{2.5}$ and PM_{10} exceeded NAAQS-CN, respectively. The results suggested that both BC and PMs levels in Nanjing have decreased because of energy conservation since 2014. The average concentration of O_3 was 37.7 ppb with 40 days of exceedance. Precursor concentrations, including CO, NO_x and NO_y, averaged 753, 28.4, and 28.6 ppb, respectively. Contrast to particles, O_3 concentration has increased in urban Nanjing, implying a severer pollution in rural area and entire YRD region. All the aerosols have substantially monthly and diurnal variations. Both particles and precursors reached maximum values in December and minimum values in October due to higher emission and less precipitation. O_3 showed a peak in September because of stronger radiation. Diurnal variations of BC and PMs were similar with peaks around 7:00~9:00 and 22:00~0:00 LT. Both of the peaks were influenced by traffic emissions in rush hours and accumulation of air pollution especially at night-time. The peaks of PMs often occurred 1~ 2 h later than those of BC, possibly due to the production of secondary particles. Precursors and particles varied similarly in time, and the diurnal variation of O_3 was analogous to that of radiation with peak around 15:00 LT.

624

625 $PM_{2.5}$ has a quasi-power-law distribution with Vis under RH of different ranges. The correlation is
626 stronger than that in a rural region in YRD, implying greater effects of air pollution on visibility in
627 urban Nanjing. O_3 shows an anti-correlation with NO_x generally, but it tends to be positive with a
628 relatively high temperature and low level of NO_x. $PM_{2.5}$ and BC are overall negatively correlated
629 with O_3. A positive correlation between $PM_{2.5}$ and O_3 exists under high temperatures, while it is not
630 found in BC-O_3 correlation. The negative correlation is related to the titration effect of high NO
631 concentration, which is highly correlated with particles due to similar emission sources. And the
632 negative correlation between $PM_{2.5}$ and UV suggests particles could decrease actinic flux of
633 radiation, and thus inhibit the photolysis reactions near surface to degrees. The positive correlation
634 implies the formation of secondary aerosols under the effects of the high concentrations of oxidants
635 and solar radiation. BC is hard to be generated through chemical reactions, which might explain
636 why the correlation between BC and O_3 is obscurer when temperature rises. An increase in CO, as
637 well as $PM_{2.5}$ and BC, always results in higher O_3 concentration, while NO_x reverses, which
638 indicates a VOC-sensitive regime for photochemical production of O_3 in urban Nanjing.

639

640 Backward trajectories indicate that Nanjing could be affected by local air flow (35% in DJF) and
641 long-distance air flows mostly from western (11% in SON), northwestern (31% in DJF), northern
642 (up to 50 % in SON and DJF), eastern (40% in SON and 17% in DJF). Considerable air pollution
643 in the urban area of Nanjing is due to local and sub-regional emissions. Basically, air masses from
644 the oceans and remote or less-developed areas are relatively clean with low aerosols concentrations.
645 α_{ts} at the site is usually low when the relative humidity of air masses is high, possibly suggesting

the increased hygroscopicity and more secondary aerosols production under higher RH.

A case study for a typical high O_3 and $PM_{2.5}$ episode in December 2016 illustrates the important influences of sub-regional transport of pollutants from strong source regions and local synoptic weather on the episode. Stable conditions such as an anticyclonic system make it easy for pollutants to accumulate in urban Nanjing. Results from this case reveal the mechanisms of sub-regional transport of primary and secondary air pollutants within the YRD region.

Overall, this work highlights the interactions and mechanisms of various aerosols and metrological fields besides the important environmental impact from human activities and meteorological conditions in the urban area in YRD region. Considering both results in this study and previous work, it is suggested that collaborative control measures among different administrative regions are urgently needed including but not limited to energy conservation and reduction of pollution emissions to improve air quality in the western part of YRD region.

Data availability. The GDP data is from http://www.njtj.gov.cn/. Satellite CO data are available at: https://gmao.gsfc.nasa.gov/reanalysis/MERRA. The aerosols AOD data are available at: https://giovanni.gsfc.nasa.gov/giovanni. The Lagrangian dispersion model Hybrid Single-Particle Lagrangian Integrated Trajectory (HYSPLIT) was supplied by NOAA: http://ready.arl.noaa.gov/HYSPLIT_traj.php. The meteorological data for HYSPLIT are accessible from ftp://arlftp.arlhq.noaa.gov/pub/archives/gdas1.

Competing interests. The authors declare that they have no conflict of interest.

Author Contributions. Huimin Chen, Bingliang Zhuang and Tijian Wang designed research; Huimin Chen, Bingliang Zhuang, Jane Liu, and Shu Li performed research; Huimin Chen, Bingliang Zhuang, Min Xie, Mengmeng Li, Pulong Chen and Ming Zhao analyzed data; and Huimin Chen, Bingliang Zhuang, and Jane Liu wrote the paper.

Acknowledgements. This work was supported by the National Program of China (2017YFC0209803, 2014CB441203, 2016YFC0203303), the National Natural Science Foundation of China (41675143, 91544230, 41621005). The authors would like to thank all members in the AERC of Nanjing University for maintaining instruments.

References

Allen, R. J., Sherwood, S. C., Norris, J. R., and Zender, C.S.: Recent Northern Hemisphere tropical expansion primarily driven by black carbon and tropospheric ozone, Nature, 485, doi:10.1038/nature11097, 350–353, 2012.

Anderson, T. L. and Ogren, J. A.: Determining aerosol radiative properties using the TSI 3563 integrating nephelometer, Aerosol Sci. Tech., 29, 57–69, 1998.

An, J., Zou, J., Wang, J., Lin, X., Zhu, B., 2015. Differences in ozone photochemical characteristics between the megacity Nanjing and its suburban surroundings, Yangtze River Delta, China.

689 Environ. Sci. Pollut. Res. 22, 19607–19617.
690 Arnott, W. P., Hamasha, K., Moosmuller, H., Sheridan, P. J., and Ogren, J. A.: Towards aerosol light-
691 absorption measurements with a 7-wavelength aethalometer: evaluation with a photoacoustic
692 instrument and 3-wavelength nephelometer, Aerosol Sci. Technol., 39, 17–29,
693 doi:10.1080/027868290901972, 2005.
694 Atkinson, R.: Atmospheric chemistry of VOCs and NOx, Atmos.Environ., 34, 2063–2101,
695 doi:10.1016/S1352-2310(99)00460-4, 2000.
696 Badarinath, K. V. S., Kharol, S. K., Chand, T. R. K., Parvathi, Y. G., Anasuya, T., and Jyothsna, A.
697 N.: Variations in black carbon aerosol, carbon monoxide and ozone over an urban area of
698 Hyderabad, India, during the forest fire season, Atmos. Res., 85(1), 18–26, 2007.
699 Baker, A. K., Beyersdorf, A. J., Doezema, L. A., Katzenstein, A., Meinardi, S., Simpson, I. J., Blake,
700 D. R., Rowland, F. S.: Measurements of nonmethane hydrocarbons in 28 United States cities,
701 Atmos. Environ., 2008, 42(1): 170–182.
702 Chameides, W. L., Li, X., Tang, X., Zhou, X., Luo, C., Kiang, C. S., John, J. St., Saylor, R. D., Liu,
703 S. C., Lam, K. S., Wang, T., and Giorgi, F.: Is ozone pollution affecting crop yields in China,
704 Geophys. Res. Lett., 26, 867–870, 1999b.
705 Chameides, W. L., Yu, H., Liu, S. C., Bergin, M., Zhou, X., Mearns, L., Wang., G., Kiang, C. S.,
706 Saylor, R. D., Luo, C., Huang, Y., Steiner, A., and Giorgi, F.: Case study of the effects of
707 atmospheric aerosols and regional haze on agriculture: An opportunity to enhance crop yields in
708 China through emission controls?, PNAS, 96, 13626–13633, 1999a.
709 Chen, T.; He, J.; Lu, X.W.; She, J.F.; Guan, Z.Q. Spatial and Temporal Variations of PM2.5 and Its
710 Relation to Meteorological Factors in the Urban Area of Nanjing, China. Int. J. Environ. Res.

711 Public Health 2016, 13, 921.
712 Cheung, V.T.F., Wang, T., 2001. Observational study of ozone pollution at a rural site in the Yangtze
713 Delta of China. Atmos. Environ. 35, 4947–4958.
714 Chow, J. C., Watson, J. G., Lowenthal, D. H., Chen, L.-W. A., Motallebi, N.: PM2.5 source profiles
715 for black and organic carbon emission inventories. Atmospheric Environment, 2011, 45(31):
716 5407-5414.
717 Collaud Coen, M., Weingartner, E., Apituley, A., Ceburnis, D., Fierz-Schmidhauser, R., Flentje, H.,
718 Henzing, J. S., Jennings, S. G., Moerman, M., Petzold, A., Schmid, O., and Baltensperger, U.:
719 Minimizing light absorption measurement artifacts of the Aethalometer: evaluation of five
720 correction algorithms, Atmos. Meas. Tech., 3, 457–474, doi:10.5194/amt-3-457-2010, 2010.
721 Deng, J. J., Wang, T.J., Liu, L., Jiang, F.: Modeling heterogeneous chemical processes on aerosol
722 surface. Particuology 8 (4), 308-318, 2010.
723 Deng, J., Wang, T., Jiang, Z., Xie, M., Zhang, R., Huang, X., Zhu, J., 2011. Characterization of
724 visibility and its affecting factors over Nanjing, China. Atmospheric Research 101, 681-691.
725 Derwent, R. G., Ryall, D. B., Jennings, S. G., Spain, T. G., and Simmonds, P. G.: Black carbon
726 aerosol and carbon monoxide in European regionally polluted air masses at Mace Head, Ireland
727 during 1995–1998, Atmos. Environ., 35(36), 6371–6378, 2001.
728 Ding, A. J., Fu, C. B., Yang, X. Q., Sun, J. N., Zheng, L. F., Xie, Y. N., Herrmann, E., Nie, W., Petaja,
729 T., Kerminen, V. -M., and Kulmala, M.: Ozone and fine particle in the western Yangtze River Delta:
730 an overview of 1 yr data at the SORPEs station, Atmos. Chem. Phys., 13, 5813–5830, 2013b.
731 Draxler, R. R. and Hess, G. D.: An overview of the HYSPLIT 4 modeling system for trajectories
732 dispersion and deposition, Aust. Meteoro. Mag., 47, 295–308, 1998.
733 Draxler, R.R. and Rolph, G.D. (2013) HYSPLIT (HYbrid Single-Particle Lagrangian Integrated
734 Trajectory) Model Access Via NOAA ARL READY Website, NOAA Air Resources Laboratory,

735 Silver Spring, MD [online].
736 Eichler, H., Cheng, Y. F., Birmili,W., Nowak, A.,Wiedensohler, A., Brüggemann, E., Gnauk, T.,
737 Herrmann, H., Althausen, D., Ansmann, A., Engelmann, R., Tesche, M., Wendisch, M., Zhang, Y.
738 H., Hu, M., Liu, S., and Zeng, L. M.: Hygroscopic properties and extinction of aerosol particles at
739 ambient relative humidity in South-Eastern China, Atmos. Environ., 42, 25, 6321–6334.
740 doi:10.1016/j.atmosenv.2008.05.007, 2008.
741 Gao, J., Wang, T., Ding, A., Liu, C.: Observational study of ozone and carbon monoxide at the
742 summit of mount Tai (1534 m a.s.l.) in central-eastern China. Atmos. Environ., 2005, 39(26),
743 4779–4791.
744 Geng, F. H., Tie, X. X., Xu, J. M., Zhou, G. Q., Peng, L., Gao, W., Tang, X., Zhao, C. S.:
745 Characterizations of ozone, NOx, and VOCs measured in Shanghai, China. Atmos. Environ. 42,
746 6873–6883, 2008.
747 Gong, W., Zhang, T.H., Zhu, Z.M., Ma, Y.Y, Ma, X., Wang, W.: Characteristics of PM1.0, PM2.5
748 and PM10 and their relation to black carbon in Wuhan, central China. Atmosphere, 2015, 6(9):
749 1377-1387.
750 Guo, H., Wang, T., Simpson, I., Blake, D., Yu, X., Kwok, Y., et al., 2004b. Source contributions to
751 ambient VOCs and CO at a rural site in eastern China. Atmos. Environ. 38, 4551–4560.
752 Han, S., 2011. Analysis of the relationship between O3, NOandNO2 in Tianjin, China. Aerosol Air
753 Qual. Res.
754 Huang, F., Li, X., Wang, C., Xu, Q., Wang, W., Luo, Y., Tao, L., Gao, Q., Guo, J., Chen, S.: PM2.5
755 spatiotemporal variations and the relationship with meteorological factors during 2013–2014 in
756 Beijing, China. PLoS ONE 2015, 10, e0141642.
757 Huang, X., Li, M., Li, J., Song, Y.: A high-resolution emission inventory of crop burning in fields
758 in China based on MODIS Thermal Anomalies/Fire products. Atmospheric Environment, 2012,
759 50:9-15.
760 Huang, X. X., Wang, T. J., Jiang, F., Liao, J. B., Cai, Y. F., Yin, C. Q., Zhu, J. L., Han, Y., 2013.

761 Studies on a severe dust storm in East Asia and its impact on the air quality of Nanjing, China.
762 Aerosol Air Qual. Res. 13, 179e193.
763 Jennings, S. G., Spain, T. G., Doddridge, B. G., Maring, H., Kelly,B. P., and Hansen, A. D. A.:
764 Concurrent measurements of black carbon aerosol and carbon monoxide at Mace Head, J. Geophys.
765 Res. Atmos., 101(D14), 19447–19454, 1996.
766 Jerrett, M., Finkelstein, M. M., Brook, J. R., Arain, M. A., Kanaroglou, P., Stieb, D. M., Gilbert, N.
767 L., Verma, D., Finkelstein, N., Chapman, K. R., and Sears, M. R.: A Cohort Study of Traffic-
768 Related Air Pollution and Mortality in Toronto, Ontario, Canada. Environmental Health
769 Perspectives, 2009, 117(5):772-777.
770 Jiang, J., Zheng, Y. F., Liu, J. J., and Fan, J. J.: Observational research on planetary boundary layer
771 by lidar over Nanjing city. Environ. Sci. Technol. 37, 22–27 (in Chinese), 2014.
772 Jiang, L., Zhang, Z. F., Zhu, B., Shen, Y., Wang, H. L., Shi, S. S., Sha, D. D.: Comparison of
773 parameterizations for the atmospheric extinction coefficient in Lin'an, China. The Science of the
774 total environment., 2018, 621. 507-515. 10.1016/j.scitotenv.2017.11.182.
775 Khoder, M. I.: Atmospheric conversion of sulfur dioxide to particulate sulfate and nitrogen dioxide
776 to particulate nitrate and gaseous nitric acid in an urban area, Chemosphere, 49, 675–684, 2002.
777 Kristjánsson, J.E., 2002. Studies of the aerosol indirect effect from sulfate and black carbon aerosols.
778 Journal of Geophysical Research 107 (D15), 4246.
779 Kumar, R., Barth, M.C., Madronich, S., Naja, M., Carmichael, G.R., Pfister, G.G., Knote, C.,
780 Brasseur, G.P., Ojha, N., Sarangi, T., 2014. Effects of dust aerosols on tropospheric chemistry
781 during a typical pre-monsoon season dust storm in northern India. Atmos. Chem. Phys. 14, 6813-
782 6834.
783 Larson, S.M., and Cass, G.R.: Characteristics of summer midday low-visibility events in the Los

784 Angeles area. Environmental Science & Technology. 23-281, 1989.

785 Liao, H., Seinfeld, J.H., 2005. Global impacts of gas-phase chemistry aerosol interactions on direct
786 radiative forcing by anthropogenic aerosols and ozone. Journal of Geophysical Research 110,
787 D18208.

788 Li, G. H., Zhang, R. Y., Fan, J. W.: Impacts of black carbon aerosol on photolysis and ozone. Journal
789 of Geophysical Research., 2005, 110(D23206).

790 Li, J., Bo, Y., Xie, S.: Estimating emissions from crop residue open burning in China based on
791 statistics and MODIS fire products. Journal of Environmental Sciences, 2016, 44:158-167.

792 Li, J., Wang, Z., Wang, X., Yamaji, K., Takigawa, M., Kanaya, Y., Pochanart, P., Liu, Y., Irie, H.,
793 Hu, B., Tanimoto, H., and Akimoto, H.: Impacts of aerosols on summertime tropospheric
794 photolysis frequencies and photochemistry over Central Eastern China, Atmos. Environ., 45,
795 1817–1829, doi:10.1016/j.atmosenv.2011.01.016, 2011.

796 Li, M., Wang, T., Xie, M., Li, S., Zhuang, B., Chen, P.: Agricultural fire impacts on ozone
797 photochemistry over the Yangtze River Delta region, East China. Journal of Geophysical
798 Research: Atmospheres, 2018.

799 Li, M., Wang, T., Xie, M., Li, S., Zhuang, B., Chen, P.: Impacts of aerosol-radiation feedback on
800 local air quality during a severe haze episode in Nanjing megacity, eastern China, Tellus B:
801 Chemical and Physical Meteorology, 2017, 69(1):1339548.

802 Li, M., Zhang, Q., Kurokawa, J., Woo, J.-H., He, K. B., Lu, Z. F., Ohara, T., Song, Y., Streets, D.
803 G., Carmichael, G. R., Cheng, Y. F., Hong, C. P., Huo, H., Jiang, X. J., Kang, S., Liu, F., Su, H.,
804 Zheng, B.: MIX: a mosaic Asian anthropogenic emission inventory under the international
805 collaboration framework of the MICS-Asia and HTAP, Atmos. Chem. Phys., 2017, 17, 935–963.

806 Lin, W., Xu, X., Zhang, X., Tang, J., 2008. Contributions of pollutants from North China Plain to
807 surface ozone at the Shangdianzi GAW Station. Atmos. Chem. Phys. 8, 5889–5898.

808 Liu, P. F., Zhao, C. S., Gobel, T., Hallbauer, E., Nowak, A., Ran, L., Xu, W. Y., et al.: Hygroscopic
809 properties of aerosol particles at high relative humidity and their diurnal variations in the North
810 China Plain, Atmos. Chem. Phys., 3479–3494, doi:10.5194/acp-11-3479-2011, 2011.

811 Luo, C., St. John, J. C., Zhou, X. J., Lam, K. S., Wang, T., and Chameides, W. L.: A nonurban ozone

812 air pollution episode over eastern China: Observation and model simulation, J. Geophys. Res., 105,
813 1889–1908, 2000.
814 Mcgowan, H. and Clark, A.: Identification of dust transport pathways from Lake Eyre, Australia
815 using Hysplit, Atmos. Environ., 42, 6915–6925, 2008.
816 Meng, Z.Y., Xu, X.B., Yan, P., Ding, G.A., Tang, J., Lin, W.L., et al., 2009. Characteristics of trace
817 gaseous pollutants at a regional background station in Northern China. Atmos.Chem. Phys. 9,
818 927–936.
819 Ministry of Environmental Protection of China (MEP), Ambient air quality standards (GB 3095–
820 2012), 12 pp., China Environmental Science Press, Beijing, 2012.
821 Müller, T., Laborde, M., Kassell, G., and Wiedensohler, A.: Design and performance of a three-
822 wavelength LED-based total scatter and backscatter integrating nephelometer, Atmos. Meas. Tech.,
823 4, 1291–1303, doi:10.5194/amt-4-1291-2011, 2011.
824 Novelli, P.C., Masari1ea, K. A., Lang, P.M.: Distributions and recent changes of carbon monoxide
825 in the lower troposphere. Journal of Geophysical Research Atmospheres, 1998, 103(D15).
826 Pan, X.L., Kanaya, Y., Wang, Z.F., Liu, Y., Pochanart, P., Akimoto, H., Sun, Y.L., Dong, H.B., Li,
827 J., Irie, H., Takigawa, M., 2011. Correlation of black carbon aerosol and carbon monoxide in the
828 high-altitude environment of Mt. Huang in Eastern China. Atmospheric Chemistry and Physics 11,
829 9735-9747.
830 Petzold, A., Kopp, C., and Niessner, R.: The dependence of the specific attenuation cross-section on
831 black carbon mass fraction and particle size, Atmos. Environ., 31, 661–672, 1997.
832 Qian, L., Yan, Y., and Qian, J.M.: An Observational Study on Physical and Optical Properties of
833 Atmospheric Aerosol in Autumn in Nanjing [J]. Meteorological and Environmental Research 2014,
834 5(2): 24 − 30
835 Roberts, P. T., Friedlander, S. K.: Analysis of sulfur in deposited aerosol particles by vaporization

836 and flame photometric detection. Atmospheric Environment, 1976, 10(5), 403-408.
837 Sassen, K., 2002. Indirect climate forcing over the western US from Asian dust storms. Geophys..
838 Res. Lett. 29.
839 Schleicher, N., Cen, K., Norra, S.: Daily variations of black carbon and element concentrations of
840 atmospheric particles in the Beijing megacity – Part 1: General temporal course and source
841 identification. Chemie der Erde - Geochemistry, 2013, 73(1):51-60.
842 Schmid, O., Artaxo, P., Arnott,W. P., Chand, D., Gatti, L. V., Frank, G. P., Hoffer, A., Schnaiter, M.,
843 and Andreae, M. O.: Spectral light absorption by ambient aerosols influenced by biomass burning
844 in the Amazon Basin. I: Comparison and field calibration of absorption measurement techniques,
845 Atmos. Chem. Phys., 6, 3443–3462, doi:10.5194/acp-6-3443-2006, 2006.
846 Shao, M., Tang, X., Zhang, Y., Li, W., 2006. City clusters in China: air and surface water pollution.
847 Front. Ecol. Environ. 4, 353–361.
848 Shen, G. F., Yuan, S. Y., Xie, Y. N., Xia, S. J., Li, L., Yao, Y. K., Qiao, Y. Z., Zhang, J., Zhao, Q.Y.,
849 Ding, A. J.: Ambient levels and temporal variations of PM2.5 and PM10 at a residential site in
850 the mega-city, Nanjing, in the western Yangtze River Delta, China. J. Environ. Sci. Health Part A
851 2014, 49, 171–178.
852 Shi, C., Wang, S., Liu, R., Zhou, R., Li, D., Wang, W., et al., 2015. A study of aerosol optical
853 properties during ozone pollution episodes in 2013 over Shanghai, China. Atmos. Res. 153, 235–
854 249.
855 Song, W.; Jia, H.; Huang, J.; Zhang, Y. A satellite-based geographically weighted regression model
856 for regional PM2.5 estimation over the Pearl River Delta region in China. Remote Sens. Environ.
857 2014, 154, 1–7.
858 Spackman, J. R., Schwarz, J. P., Gao, R. S., Watts, L. A., Thomson, D. S., Fahey, D. W., Holloway,
859 J. S., de Gouw, J. A., Trainer, M., and Ryerson, T. B.: Empirical correlations between black carbon
860 aerosol and carbon monoxide in the lower and middle troposphere, Geophys. Res. Lett., 35(19),

L19816, doi:10.1029/2008GL035237, 2008.

Stein, A. F., Draxler, R. R., Rolph, G. D., Stunder, B. J. B., Cohen, M. D., and Ngan, F.: NOAA'S Hysplit Atmospheric Transport and Dispersion Modeling System, Bull. Amer. Meteor. Soc., 96, 2059–2077. doi: http://dx.doi.org/10.1175/BAMS-D-14-00110.1, 2016.

Streets, D.G., Gupta, S., Waldhoff, S.T., Wang, M.Q., Bond, T.C., Bo, Y.Y., 2001. Black carbon emissions in China. Atmospheric Environment 35, 4281-4296.

Tegen, I., Schepanski, K.:The global distribution of mineral dust. IOP Conference Series: Earth and Environmental Science, 2009, 7:012001.

Tu, J., Xia, Z. G., Wang, H. S., and Li, W. Q.: Temporal variations in surface ozone and its precursors and meteorological effects at an urban site in China, Atmos. Res., 85, 310–337, 2007.

van Donkelaar, A., Martin, R. V., Brauer, M., Kahn, R., Levy, R., Verduzco, C., and Villeneuve, P. J.: Global estimates of ambient fine particulate matter concentrations from satellite-based aerosol optical depth: development and application, Environ. Health Perspectives, 118, 847– 855, 2010.

Verma, R.L., Sahu, L.K., Kondo, Y., Takegawa, N., Han, S., Jung, J.S., Kin, Y.J., Fan, S., Sugimoto, N., Shammaa, M.H., Zhang, Y.H., Zhao, Y., 2010. Temporal variations of black carbon in Guangzhou, China, in summer 2006. Atmospheric Chemistry and Physics 10, 6471-6485.

von Schneidemesser, E., Monks, P. S., and Plass-Duelmer, C.: Global comparison of VOC and CO observations in urban areas, Atmos. Environ., 2010, 44(39): 5053–5064.

Wang, G. H., Huang, L. M., Gao, S. X., Gao, S. T., and Wang, L.S.: Characterization of watersoluble species of PM10 and PM2.5aerosols in urban area in Nanjing, China, Atmos. Environ., 36,1299–1307, 2002.

Wang, H. L., Zhuang, Y. H., Wang, Y., Sun, Y. L., Yuan, H., Zhuang, G. S., Hao, Z. P.: Long-term monitoring and source apportionment of PM 2.5/PM 10 in Beijing, China. Journal of Environmental Sciences, 2008, 20(11): 1323-1327.

885 Wang, M., Shao, M., Chen, W., Yuan, B., Lu, S., Zhang, Q., Zeng, L., Wang, Q.: A temporally and
886 spatially resolved validation of emission inventories by measurements of ambient volatile organic
887 compounds in Beijing, China. Atmos. Chem. Phys., 2014, 14(12): 5871–5891.
888 Wang, P., Zhao, W.: Assessment of ambient volatile organic compounds (VOCs) near major roads
889 in urban Nanjing, China[J]. Atmospheric Research, 2008, 89(3):0-297.
890 Wang, M.Y., Cao, C.X., Li, G.S., and Singh, R.P.: Analysis of a severe prolonged regional haze
891 episode in the Yangtze River Delta, China, Atmos. Environ., 102, 112-121, 2015.
892 Wang, T., Cheung, V.T.F., Anson, M., Li, Y.S., 2001a. Ozone and related gaseous pollutants in the
893 boundary layer of eastern China: overview of the recent measurements at a rural site. Geophys.
894 Res. Lett. 28, 2373–2376.
895 Wang, T., Cheung, T., Li, Y., Yu, X., Blake, D., 2002. Emission characteristics of CO, NOx, SO2
896 and indications of biomass burning observed at a rural site in eastern China. J. Geophys. Res.-
897 Atmos. 107.
898 Wang, T., Poon, C.N., Kwok, Y.H., Li, Y.S., 2003. Characterizing the temporal variability and
899 emission patterns of pollution plumes in the Pearl River Delta of China. Atmos. Environ.37,
900 3539–3550.
901 Wang, T., Wong, C., Cheung, T., Blake, D., Arimoto, R., Baumann, K., et al., 2004. Relationships
902 of trace gases and aerosols and the emission characteristics at Lin'an, a rural site in eastern China,
903 during spring 2001. J. Geophys. Res.-Atmos. 109.
904 Wang, T., Xue, L. K., Brimblecombe, P., Lam, Y.F., Li, L., and Zhang, L.: Ozone pollution in China:
905 A review of concentrations, meteorological influences, chemical precursors, and effects. Science
906 of the Total Environment., 575, 1582–1596, 2017.
907 Wang, T. J., Zhuang, B. L., Li, S., Liu, J., Xie, M., Yin, C. Q., Zhang, Y., Yuan, C., Zhu, J. L., Ji, L.
908 Q., and Han, Y.: The interactions between anthropogenic aerosols and the East Asian summer
909 monsoon using RegCCMS. J. Geophys. Res. Atmos., 120, doi:10.1002/2014JD022877, 2015.

910 Wang, X., Li, J., Zhang, Y., Xie, S., Tang, X., 2009b. Ozone source attribution during a severe
911 photochemical smog episode in Beijing, China. Sci. China, Ser. B: Chem. 52, 1270–1280.
912 Wang, Y. Q., Stein, A. F., Draxler, R. R., de la Rosa, J. D., Zhang, X.Y.: Global sand and dust storms
913 in 2008: Observation and HYSPLIT model verification, Atmos. Environ., 45, 6368-6381, 2011.
914 Wang, Y., Ying, Q., Hu, J., Zhang, H.: Spatial and temporal variations of six criteria air pollutants
915 in 31 provincial capital cities in China during 2013–2014. Environment International, 2014,
916 73:413–422.
917 Wang, Y., Wang, X., Kondo, Y., Kajino, M., Munger, J.W., Hao, J., 2011b. Black carbon and its
918 correlation with trace gases at a rural site in Beijing: top-down constraints from ambient
919 measurements on bottom-up emissions. Journal of Geophysical Research 116, D24304.
920 Wang, Y., Zhuang, G. S., Zhang, X. Y., Huang, K., Xu, Chang, Tang, A. H., Chen, J. M., and An, Z.
921 S.: The ion chemistry, seasonal cycle, and sources of PM2.5 and TSP aerosol in Shanghai, Atmos.
922 Environ., 40, 2935–2952, 2006.
923 Wang, Z., Li, J., Wang, X., Pochanart, P., Akimoto, H.: Modeling of Regional High Ozone Episode
924 Observed at Two Mountain Sites (Mt. Tai and Huang) in East China[J]. Journal of Atmospheric
925 Chemistry, 2006, 55(3):253-272.
926 Wang, Z., Li, Y., Chen, T., Zhang, D., Sun, F., Pan, L.: Spatial-temporal characteristics of PM2.5 in
927 Beijing in 2013. Acta Geogr. Sin. 2015, 70, 110–120.
928 Weingartner, E., Saathoff, H., Schnaiter, M., Streit, N., Bitnar, B., and Baltensperger, U.: Absorption
929 of light by soot particles: determination of the absorption coefficient by means of aethalometers,
930 J. Aerosol Sci., 34, 1445–1463, doi:10.1016/S0021- 8502(03)00359-8, 2003.
931 Wu, D., Liu, Q., Lian, Y., Bi, X., Li, F., Tan, H., Liao, B., Chen, H., Hazy weather formation and
932 visibility deterioration resulted from fine particulate (PM2.5) pollutions in Guangdong and
933 Hong Kong. J. Environ. Sci. Circumst. 2012, 32, 2660–2669.

Wu, Y.; Guo, J.; Zhang, X.; Tian, X.; Zhang, J.; Wang, Y.; Duan, J.; Li, X. Synergy of satellite and ground based observations in estimation of particulate matter in eastern China. Sci. Total Environ. 2012, 433, 20–30.

Xiao, Z., Bi, X., Feng, Y., Wang, Y., Zhou, J., Fu, X., Weng, Y., 2012. Source apportionment of ambient PM10 and PM2.5 in urban area of Ningbo City. Res. Environ. Sci. (China) 5, 549–555.

Xiao, Z. M., Zhang, Y. F., Hong, S. M., Bi, X. H., Jiao, L., Feng, Y. C., Wang, Y. Q.: Estimation of the Main Factors Influencing Haze, Based on a Long-term Monitoring Campaign in Hangzhou, China. Aerosol & Air Quality Research., 2011, 11, 873-882.

Xie, M., Zhu, K.G., Wang, T.J., Chen, P.L., Han, Y., Li, S., Zhuang, B.L., and Shu, L., Temporal characterization and regional contribution to O3 and NOx at an urban and a suburban site in Nanjing, China. Science of the Total Environment., 551–552, 533–545, 2016

Xue, L., Wang, T., Louie, P.K.K., Luk, C.W.Y., Blake, D.R., Xu, Z., 2014a. Increasing external effects negate local efforts to control ozone air pollution: a case study of Hong Kong and implications for other Chinese cities. Environ. Sci. Technol. 48, 10769–10775.

Yang, S. J., He, H. P, Lu, S. L., Chen, D., Zhu, J. X.: Quantification of crop residue burning in the field and its influence on ambient air quality in Suqian, China. Atmospheric Environment, 2008,42(9):1961-1969.

Yan, S.; Cao, H.; Chen, Y.; Wu, C.; Hong, T.; Fan, H. Spatial and temporal characteristics of air quality and air pollutants in 2013 in Beijing. Environ. Sci. Pollut. Res. 2016, 23, 1–12.

Yin, S., Wang, X.F, Xiao, Y., Tani, H., Zhong, G.S., Sun, Z.Y.: Study on spatial distribution of crop residue burning and PM2.5 change in China. Environmental Pollution, 2016, 220(Pt A):204-221.

Yi, R., Wang, Y.L., Zhang, Y.J., Shi, Y., Li, M.S., 2015. Pollution characteristics and influence factors of ozone in Yangtze River Delta. Acta Sci. Circumst. 35, 2370–2377 (in Chinese).

Yu, J., Wang, W., Zhou, J., Xu, D., Zhao, Q., He, L., 2015. Analysis of pollution characteristics and sources of PM2.5 in winter of Ningbo City. Environ. Sci. Technol. (China) 8, 150–155.

959 Zhang, Q., Streets, D.G., Carmichael, G.R., He, K.B., Huo, H., Kannari, A., Klimont, Z., Park, I.S.,
960 Reddy, S., Fu, J.S., Chen, D., Duan, L., Lei, Y., Wang, L.T., Yao, Z.L., 2009. Asian emissions in
961 2006 for the NASA INTEX-B mission. Atmos. Chem. Phys. 9, 5131–5153.
962 Zhang, Y. H., Hu, M., Zhong, L. J., Wiedensohler, A., Liu, S. C., Andreae, M. O., Wang, W., Fan, S.
963 J.: Regional integrated experiments on air quality over Pearl River Delta 2004 (PRIDE-PRD2004):
964 overview. Atmos. Environ. 42, 6157–6173, 2008.
965 Zhang, X. Y., Wang, Y. Q., Niu, T., Zhang, X. C., Gong, S.L., Zhang, Y.M., Sun, T.Y., 2012.
966 Atmospheric aerosol compositions in China: spatial/temporal variability, chemical signature,
967 regional haze distribution and comparisons with global aerosols. Atmospheric Chemistry and
968 Physics 12, 779-799.
969 Zhang, X.Y., Wang, Y.Q., Zhang, X.C., Guo, W., Gong, S.L., 2008. Carbonaceous aerosol
970 composition over various regions of China during 2006. Journal of Geophysical Research 113,
971 D14111.
972 Zhang, Y. L., Cao, F. Fine particulate matter (PM2.5) in China at a city level. Sci. Rep. 2015, 5,
973 14884.
974 Zhang, Y., Shao, K., Tang, X., 1998. The study of urban photochemical smog pollution in China.
975 Acta Scientiarum Naturalium-Universitatis Pekinensis 34, 392–400.
976 Zheng, J., Zhong, L., Wang, T., Louie, P.K.K., Li, Z., 2010. Ground-level ozone in the Pearl River
977 Delta region: analysis of data from a recently established regional air quality monitoring network.
978 Atmos. Environ. 44, 814–823.
979 Zhu, J. L., Wang, T. J., Talbot, R. H., Mao, H. T., Hall, C. B., Yang, X. Q., Fu, C. B., Zhuang, B. L.,
980 Li, S., Han, Y., Huang, X., 2012. Characteristics of atmospheric Total Gaseous Mercury (TGM)
981 observed in urban Nanjing, China. Atmospheric Chemistry and Physics 12, 12103-12118.

Zhuang, B.L., Liu, L., Shen, F.H., Wang, T.J., Han, Y., 2010. Semidirect radiative forcing of internal mixed black carbon cloud droplet and its regional climatic effect over China. Journal of Geophysical Research 115, D00K19.

Zhuang, B. L., Liu, Q., Wang, T. J., Yin, C. Q., Li, S., Xie, M., Jiang, F., Mao, H.T., 2013. Investigation on semi-direct and indirect climate effects of fossil fuel black carbon aerosol over China. Theoretical and Applied Climatology 114, 651-672.

Zhuang, B. L., Li, S., Wang, T. J., Deng, J. J., Xie, M., Yin, C. Q., and Zhu, J. L.: Direct radiative forcing and climate effects of anthropogenic aerosols with different mixing states over China, Atmos. Environ., 79, 349–361, doi:10.1016/j.atmosenv.2013.07.004, 2013b.

Zhuang, B. L., Li, S., Wang, T. J, Liu, J., Chen, H. M., Chen, P. L., Li, M. M., Xie, M.: Interaction between the Black Carbon Aerosol Warming Effect and East Asian Monsoon Using RegCM4. Journal of Climate, 2018, 31(22):9367-9388.

Zhuang, B. L., Wang, T. J., Liu, J., Li, S., Xie, M., Han, Y., Chen, P. L., Hu, Q. D., Yang X.Q., Fu, C. B., and Zhu, J. L.: The surface aerosol optical properties in the urban area of Nanjing, west GTH River Delta, China. Atmos. Chem. Phys., 17, 1143–1160, doi:10.5194/acp-17-1143-2017, 2017.

Zhuang, B. L., Wang, T. J., Liu, J., Li, S., Xie, M., Yang, X. Q., Fu, C. B., Sun, J. N., Yin, C. Q., Liao, J. B., Zhu, J. L., and Zhang, Y.: Continuous measurement of black carbon aerosol in urban Nanjing of Yangtze River Delta, China, Atmos. Environ., 89, 415–424, 2014b.

Zhuang, B. L., Wang, T. J., Liu, J., Ma, Y., Yin, C. Q., Li, S., Xie, M., Han, Y., Zhu, J. L., Yang, X. Q., and Fu, C. B.: Absorption coefficient of urban aerosol in Nanjing, west Yangtze River Delta, China, Atmos. Chem. Phys., 15, 13633–13646, doi:10.5194/acp-15-13633-2015, 2015.

Zhuang, B. L., Wang, T. J., Li, S., Liu, J., Talbot, R., Mao, H. T., Yang, X. Q., Fu, C. B., Yin, C. Q., Zhu, J. L., Che, H. Z., and Zhang, X. Y.: Optical properties and radiative forcing of urban aerosols in Nanjing, China, Atmos. Environ., 83, 43–52, 2014a.

Figure Caption

Fig 1. Time series of (a) concentrations and (b) optical properties of PM_{10}, $PM_{2.5}$, and BC from September 2016 to February 2017 at Gulou site, Nanjing, China.

Fig 2. Seasonal variations of (a) BC, (b) PM2.5, and (c) PM10. Red markers represent the monthly averages at Gulou site, Nanjing, China.

Fig 3. 6-month mean diurnal variations of BC, $PM_{2.5}$, and PM_{10} at Gulou site, Nanjing, China from September 2016 to February 2017.

Fig.4 Time series of particles from September 2016 to February 2017 at Gulou site.

Fig 5. Seasonal variations of (a) O_3, (b) NO_x, (c) CO, and (d) NO_y. The 10, 25, 50, 75, and 90% percentile values of each are shown in black, and red markers represent the monthly averages.

Fig 6. 6-month mean diurnal variations of (a) trace gases and (b) UV (ultra-violate radiation) at Gulou site from September 2016 to February 2017

Fig 7. Scatter plots of (a) O_3-NO_x color-coded with air temperature (T) and (b) $PM_{2.5}$-Vis color-coded with relative humidity (RH).

Fig 8. Scatter plots of (a) $PM_{2.5}$-O_3 and (b) BC-O_3 color-coded with air temperature (T).

Fig 9. Scatter plots of (a) O_3-UV and (b) $PM_{2.5}$-UV color coded with O_3.

Fig 10. Scatter plots of (a) CO-NO_x, (b) $PM_{2.5}$-NO_x, and (c) BC-NO_x color-coded with O_3.

Fig 11. Clusters of 96 h back trajectories arriving at the study site at 100 m in 2016 fall.

Fig 12. The 10, 25, 50, 75, and 90% percentile values in each cluster of back trajectories in 2016 fall of (a) BC, (b) $PM_{2.5}$, (c) $PM_{2.5}/PM_{10}$, (d) CO, (e) O_3, (f) NO_y, (g) α_{ts}, and (h) ω_0. Black markers represent the averages.

Fig 13. Clusters of 96 h back trajectories arriving at the study site at 100m in 2016 winter.

Fig 14. The 10, 25, 50, 75, and 90% percentile values in each cluster of back trajectories in 2016 winter of (a) BC, (b) $PM_{2.5}$, (c) $PM_{2.5}/PM_{10}$, (d) CO, (e) O_3, (f) NO_y, (g) α_{ts}, and (h) ω_0. Black markers represent the averages.

Fig 15. Time series during December 3-6, 2016, for (a) $PM_{2.5}$, BC and O_3 with associated metrological parameters, trace gases and (b) optical parameters. Red markers represent O3 over daily maximum average during winter. Weather charts on (c) 4th and (d) 5th December. (f) 96h backward trajectories analysis ending at 1200 UTC on 5th December.

Table

Table 1 Measurements at Gulou site.

Measurement		Instrument	Resolution
Meteorological parameters	T (℃)	Thermo Instruments, THOM 1405-DF	
	P (atm)	Thermo Instruments, THOM 1405-DF	
	RH (%)	Thermo Instruments, THOM 1405-DF	
	Rainfall (mm)		
	Vis (m)	Visibility Meter, GSN-1	
	UV (W/m^2)		
Particles	BC (ng/m^3)	Aethalometer, Model AE-31	1 ng/m^3
	PM2.5 ($\mu g/m^3$)	Thermo Instruments, THOM 1405-DF	0.1$\mu g/m^3$
	PM10 ($\mu g/m^3$)	Thermo Instruments, THOM 1405-DF	0.1$\mu g/m^3$
Gaseous pollutant	CO (ppb)	Thermo Instruments, TEI 48i	1 ppb
	NO_x (ppb)	Thermo Instruments, TEI 42i	0.4 ppb
	NO_y (ppb)	Thermo Instruments, TEI 42iY	0.4 ppb
	O_3 (ppb)	Thermo Instruments, TEI 49i	0.01 ppb
Optical parameters	SC (Mm^{-1})	Nephelometer, Aurora 3000	10^{-3} Mm^{-1}
	BSP (Mm^{-1})	Nephelometer, Aurora 3000	10^{-3} Mm^{-1}
	AAC (Mm^{-1})	Aethalometer, Model AE-31	10^{-3} Mm^{-1}

Table 2 Statistics of general meteorological parameters at Gulou site for the 6-month period September 2016~ February 2017.

Month	Temp (℃)	Pres (hPa)	RH (%)	Rainfall (mm)	Vis (km)	UV (W/m^2)
Sep	24.88	996.97	69.41	2.34	11.84	10.36
Oct	18.37	1003.01	85.01	3.12	9.07	5.28
Nov	12.36	1007.87	77.15	1.19	8.99	5.67
Dec	8.74	1010.53	70.33	0.81	7.61	5.03
Jan	6.49	1010.89	70.65	0.59	9.23	4.94
Feb	7.72	1009.65	59.99	0.45	10.24	7.04

Table 3 Statistics of the three particles during the study period at Gulou site, Nanjing, China

	SON	DJF	Cold seasons		
	Mean ± STD	Mean ± STD	Mean ± STD	Maximum	Minimum
BC (μg/m³)	2.126 ± 1.457	3.083 ± 1.827	2.602 ± 1.720	15.609	0.064
$PM_{2.5}$ (μg/m³)	43.1 ± 25.4	73.2 ± 40.0	58.2 ± 36.8	256.2	0.8
PM_{10} (μg/m³)	67.6 ± 39.1	105.0 ± 54.0	86.3 ± 50.8	343.4	1.1

Table 4 Statistics of trace gases during the study period

	SON	DJF	Cold seasons		
	Mean ± STD	Mean ± STD	Mean ± STD	Maximum	Minimum
CO (ppb)	753 ± 353	950 ± 388	851 ± 384	2852	176
NO_x (ppb)	21.4 ± 13.4	25.6 ± 15.5	23.5 ± 14.7	80.0	2.7
NO_y (ppb)	28.6 ± 20.5	37.0 ± 23.1	32.8 ± 22.3	158.4	3.6
O_3 (ppb)	42.3 ± 40.1	33.1 ± 24.4	37.7 ± 35.5	235.7	0.2

Table 5 Statistics of maximum and number of exceedances of O_3 and $PM_{2.5}$ compared with the National Ambient Air Quality Standards in China.

Aerosol	Mean ± STD (μg/m³)	Max (μg/m³)	N.o.E.
$PM_{2.5}$	58.2 ± 36.8	256.2	48
PM_{10}	86.3 ± 50.8	343.4	14
O_3	80.8 ± 71.8	235.7	37

N.o.E. of $PM_{2.5}$ accounts for days with 24 h average over 75 μg/m³. N.o.E. of PM_{10} accounts for days with 24 h average over 150 μg/m³. N.o.E of O_3 accounts for days with maximum 8 h average exceed 160 μg/m³.

Table 6 Statistics of aerosols at Gulou site with and without rainfall for the 6-month period

September 2016~ February 2017

	With Rainfall			Without Rainfall		
Aerosols	Mean ± STD	Maximum	Minimum	Mean ± STD	Maximum	Minimum
BC (μg/m³)	1.676 ± 1.261	8.256	0.064	2.723 ± 1.735	15.608	0.211
$PM_{2.5}$ (μg/m³)	31.2 ± 27.6	218.4	1.2	61.9 ± 36.3	256.2	0.8
PM_{10} (μg/m³)	54.3 ± 44.8	307.3	3.9	89.1 ± 47.3	319.6	4.5
CO (ppb)	659 ± 240	2194	176	876 ± 392	2852	228
NO_x (ppb)	20.4 ± 12.7	75.5	2.9	23.9 ± 14.9	80	2.7
NO_y (ppb)	25.2 ± 16.8	110.3	3.6	33.8 ± 22.8	158.4	5.2
O_3 (ppb)	22.3 ± 17.1	81.7	0.3	39.7 ± 34.6	235.7	0.2

Figure

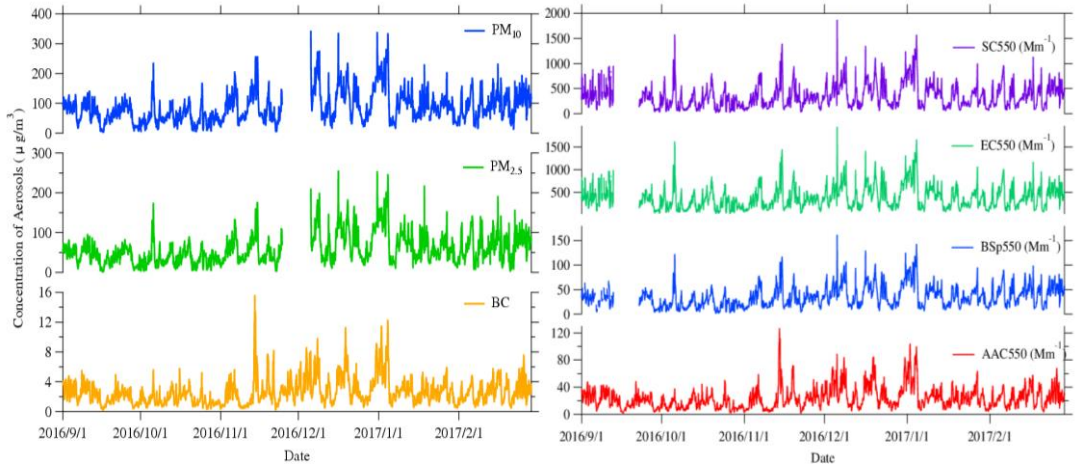

Fig 1. Time series of (a) concentrations and (b) optical properties of PM_{10}, $PM_{2.5}$, and BC from September 2016 to February 2017 at Gulou site, Nanjing, China.

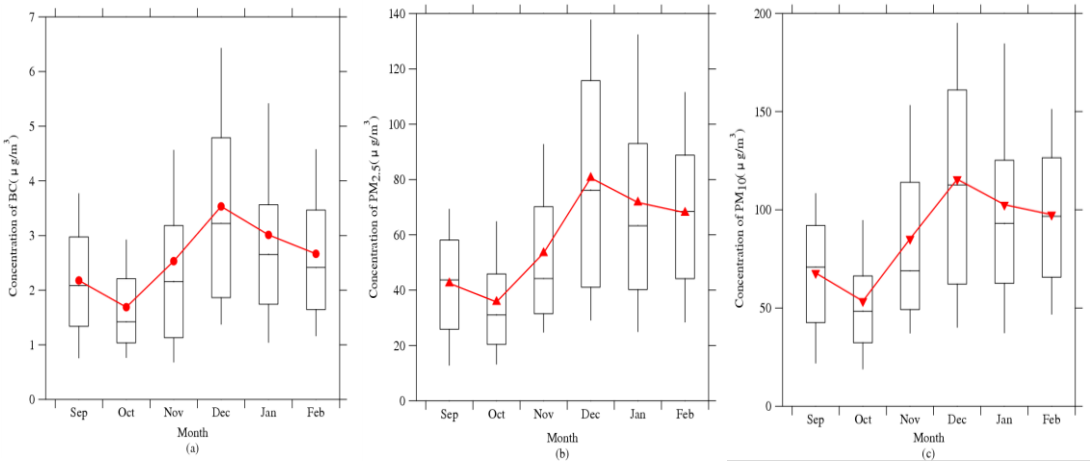

Fig 2. Seasonal variations of (a) BC, (b) $PM_{2.5}$, and (c) PM_{10}. Red markers represent the monthly averages at Gulou site, Nanjing, China.

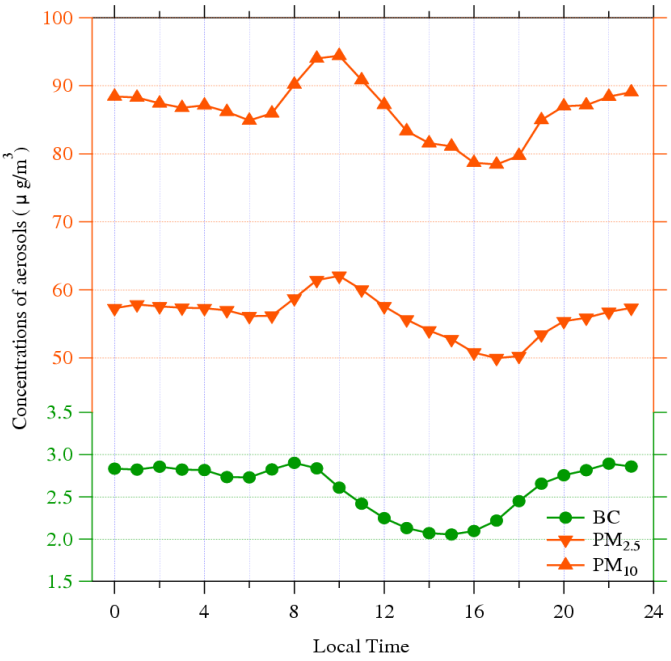

Fig 3. 6-month mean diurnal variations of BC, $PM_{2.5}$, and PM_{10} at Gulou site, Nanjing, China from September 2016 to February 2017.

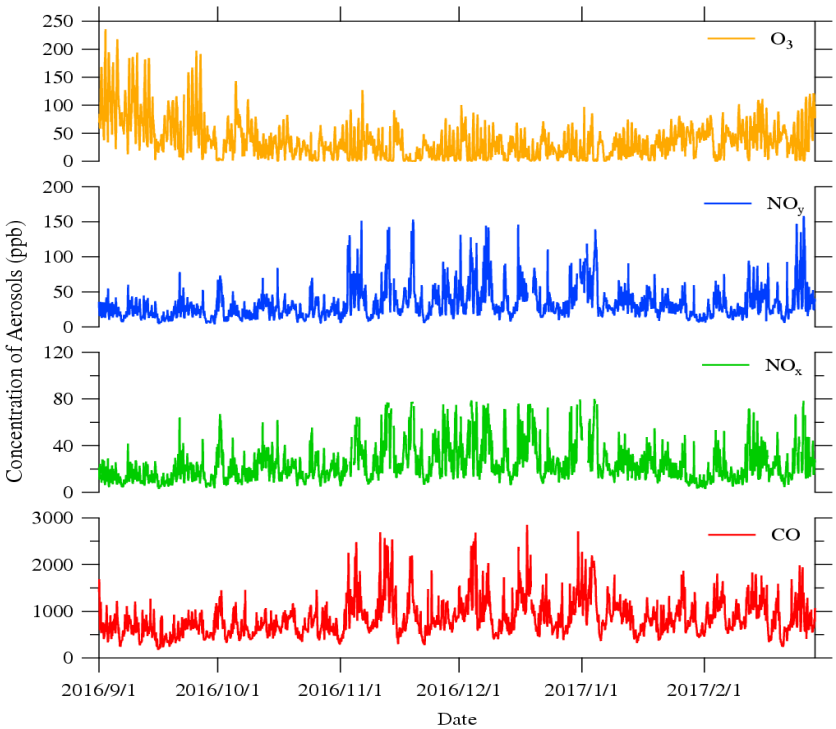

Fig.4 Time series of particles from September 2016 to February 2017 at Gulou site.

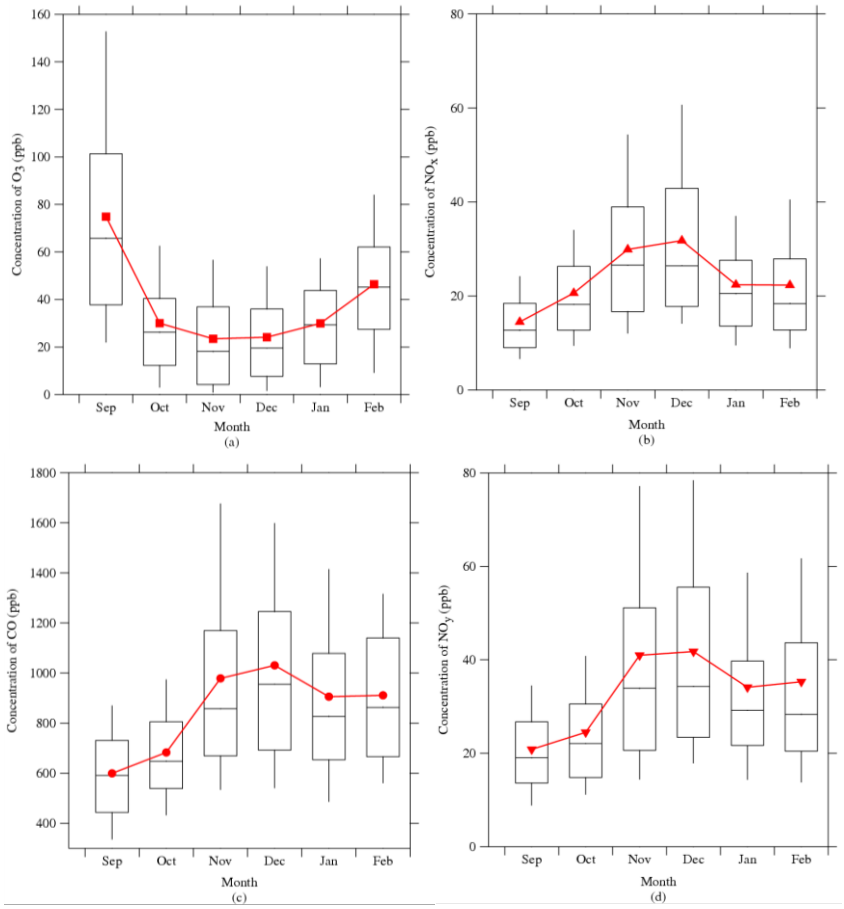

Fig 5. Seasonal variations of (a) O_3, (b) NO_x, (c) CO, and (d) NO_y. The 10, 25, 50, 75, and 90% percentile values of each are shown in black, and red markers represent the monthly averages.

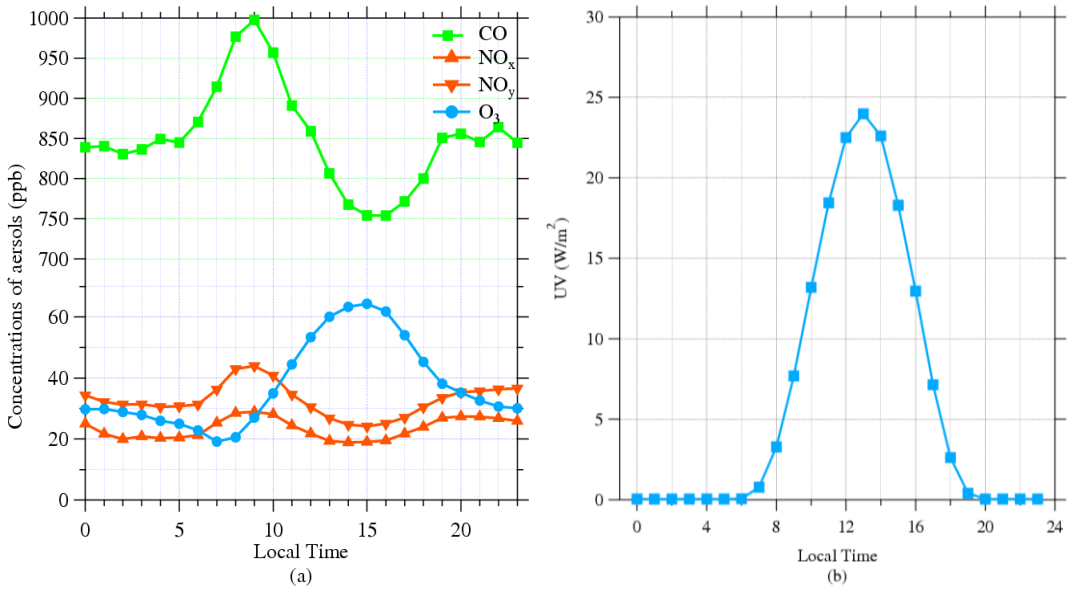

Fig 6. 6-month mean diurnal variations of (a) trace gases and (b) UV (ultra-violate radiation) at Gulou site from September 2016 to February 2017

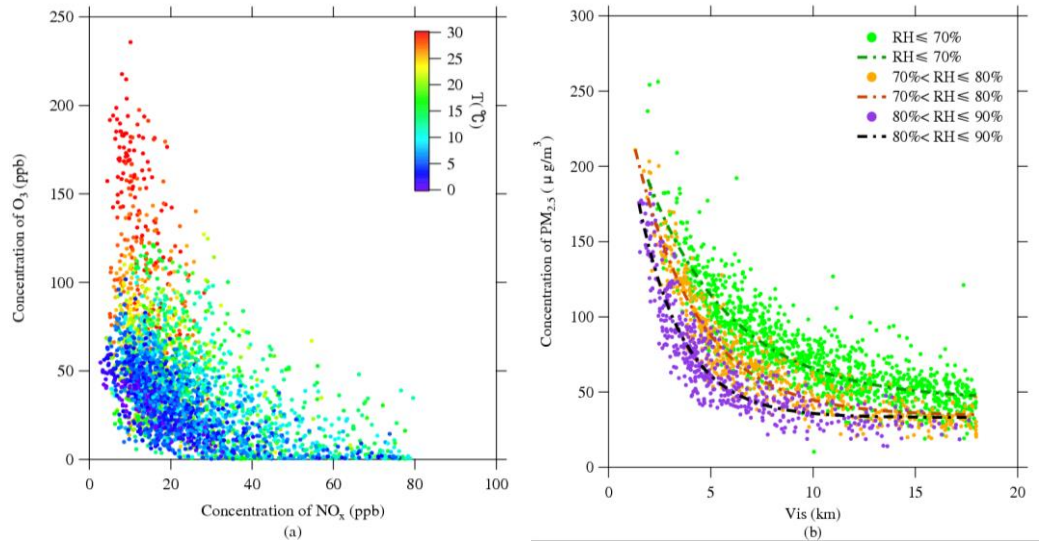

Fig 7. Scatter plots of (a) O_3-NO_x color-coded with air temperature (T) and (b) $PM_{2.5}$-Vis color-coded with relative humidity (RH).

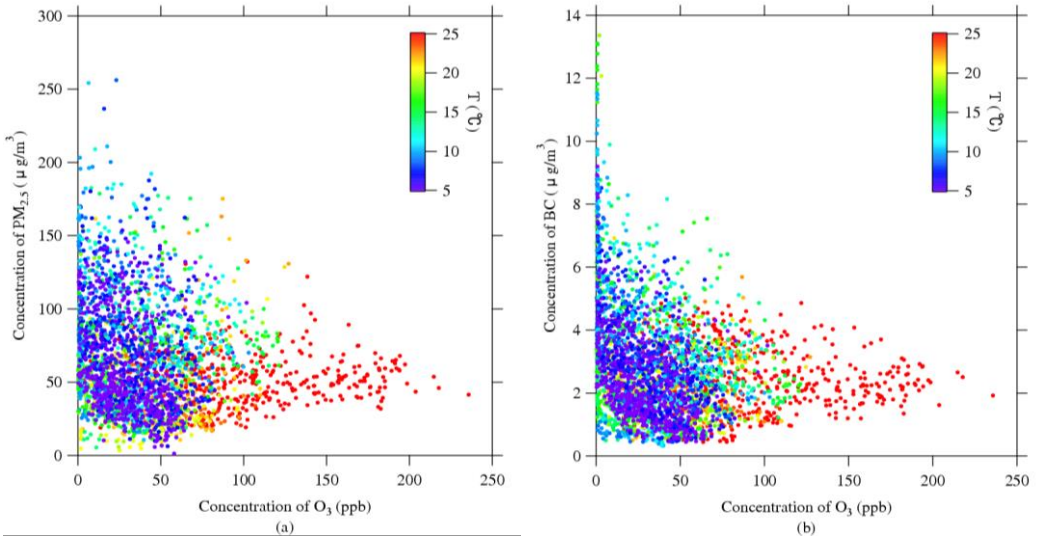

Fig 8. Scatter plots of (a) $PM_{2.5}$-O_3 and (b) BC-O_3 color-coded with air temperature (T).

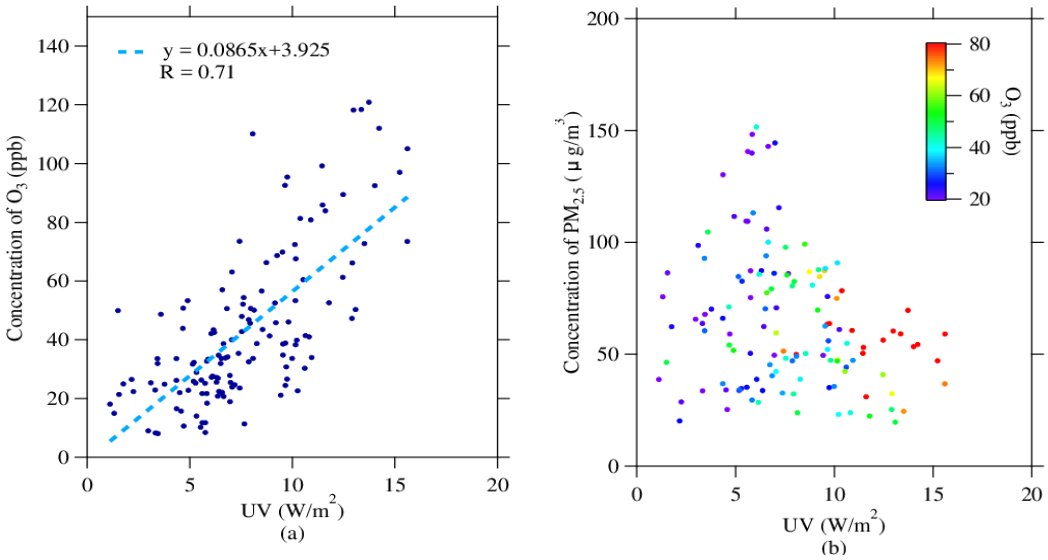

Fig 9. Scatter plots of (a) O_3-UV and (b) $PM_{2.5}$-UV color coded with O_3.

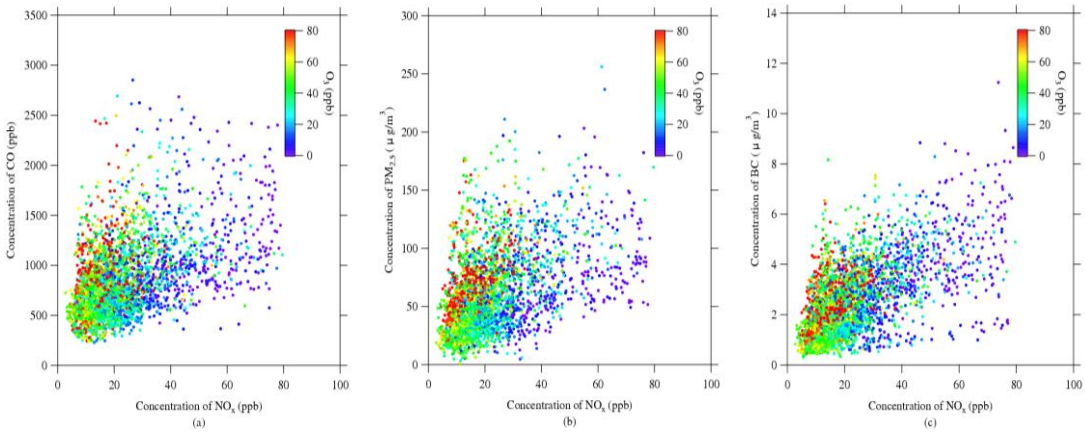

Fig 10. Scatter plots of (a) CO-NO_x, (b) $PM_{2.5}$-NO_x, and (c) BC-NO_x color-coded with O_3.

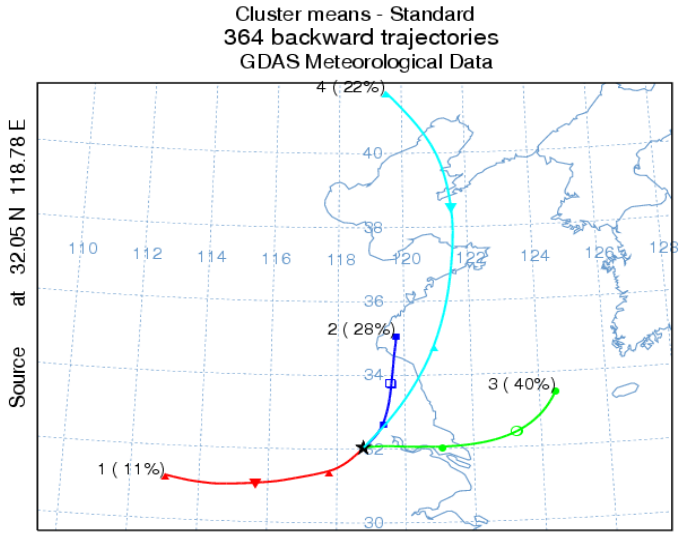

Fig 11. Clusters of 96 h back trajectories arriving at the study site at 100 m in 2016 fall.

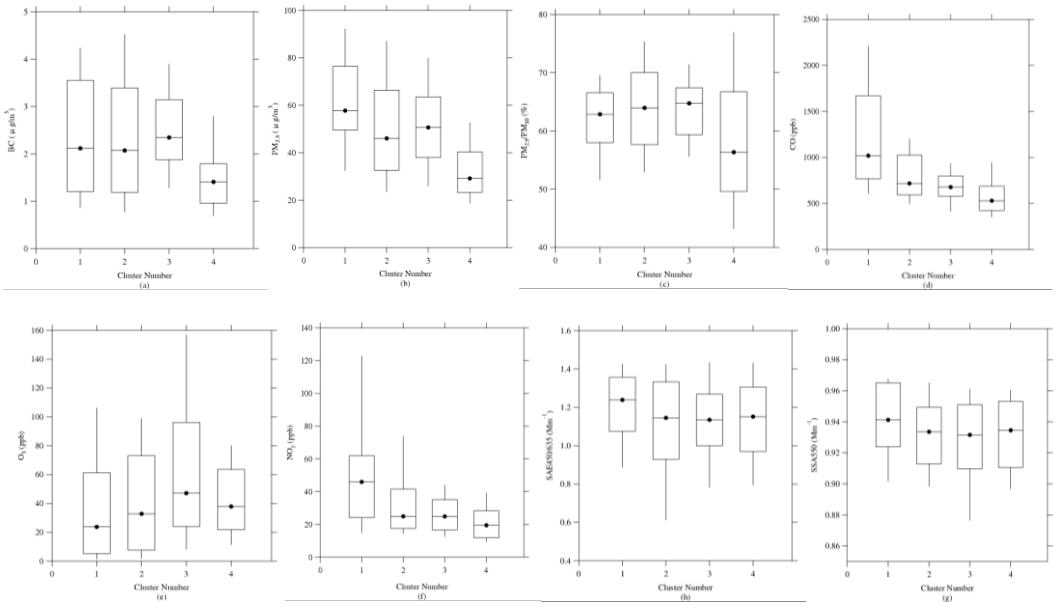

Fig 12. The 10, 25, 50, 75, and 90% percentile values in each cluster of back trajectories in 2016 fall of (a) BC, (b) $PM_{2.5}$, (c) $PM_{2.5}/PM_{10}$, (d) CO, (e) O_3, (f) NO_y, (g) α_{ts}, and (h) ω_0. Black markers represent the averages.

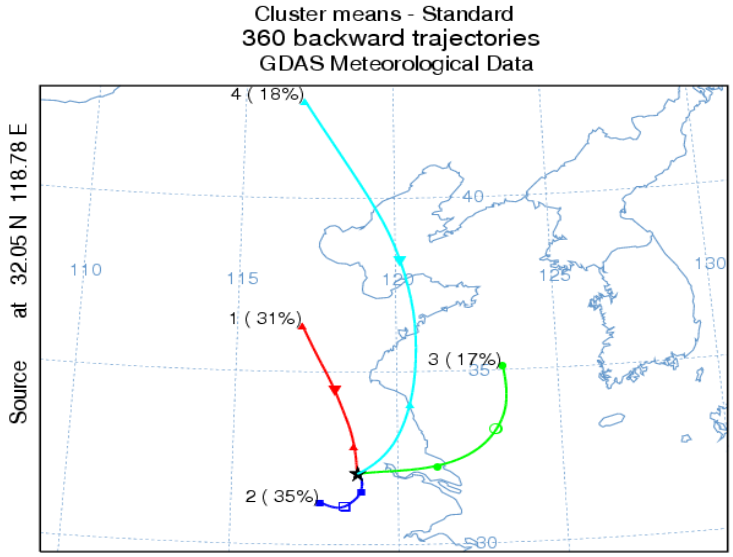

Fig 13. Clusters of 96 h back trajectories arriving at the study site at 100m in 2016 winter.

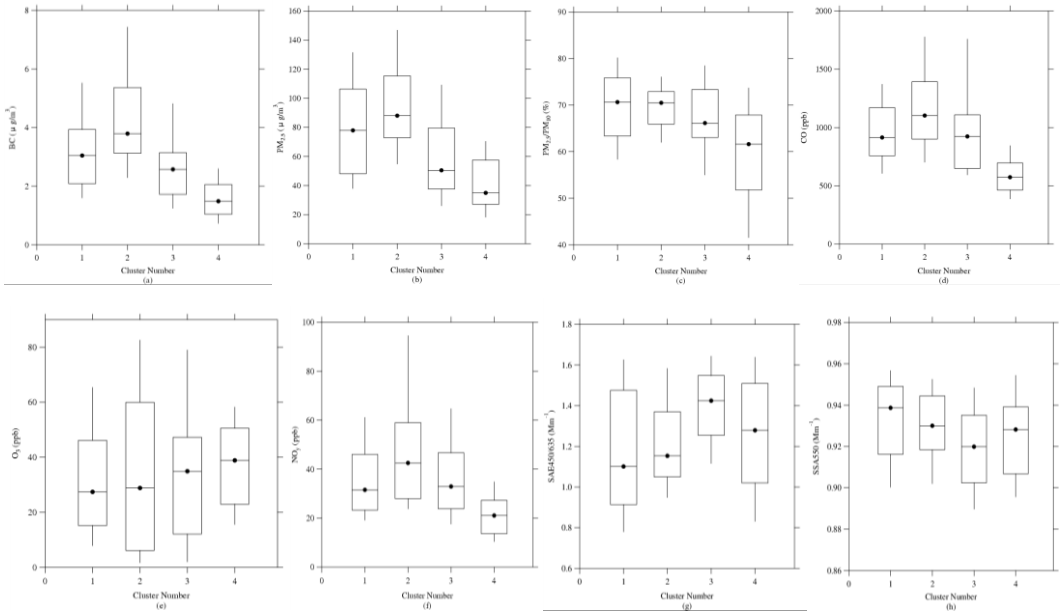

Fig 14. The 10, 25, 50, 75, and 90% percentile values in each cluster of back trajectories in 2016 winter of (a) BC, (b) $PM_{2.5}$, (c) $PM_{2.5}/PM_{10}$, (d) CO, (e) O_3, (f) NO_y, (g) α_{ts}, and (h) ω_0. Black markers represent the averages.

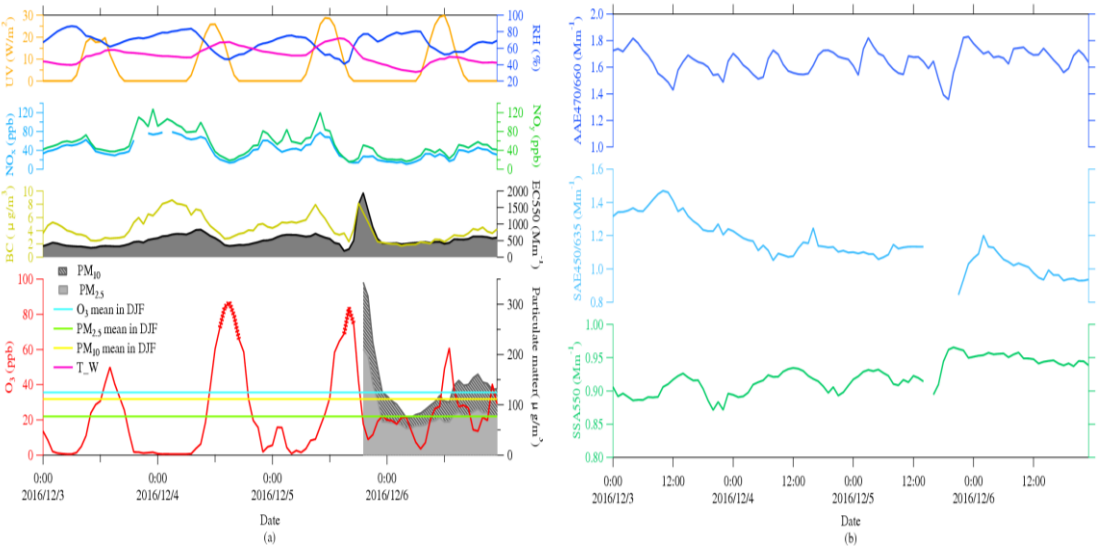

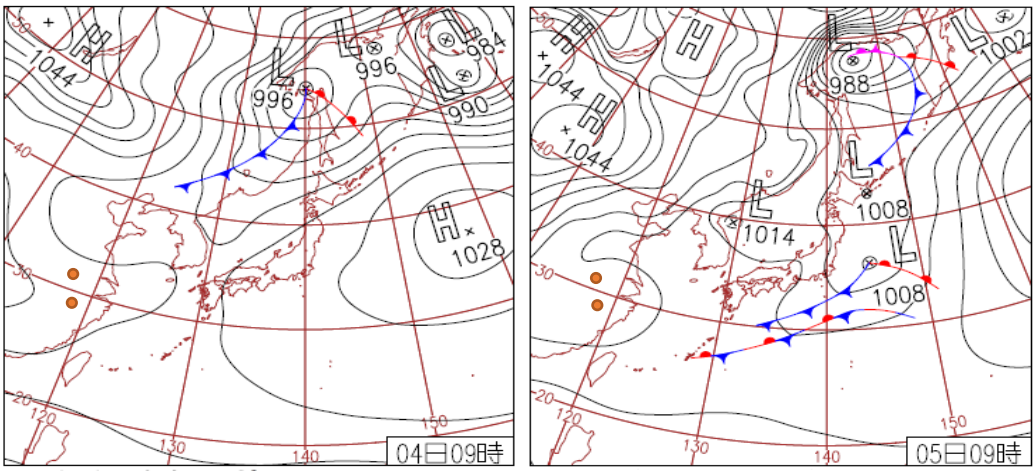

(c) (d)

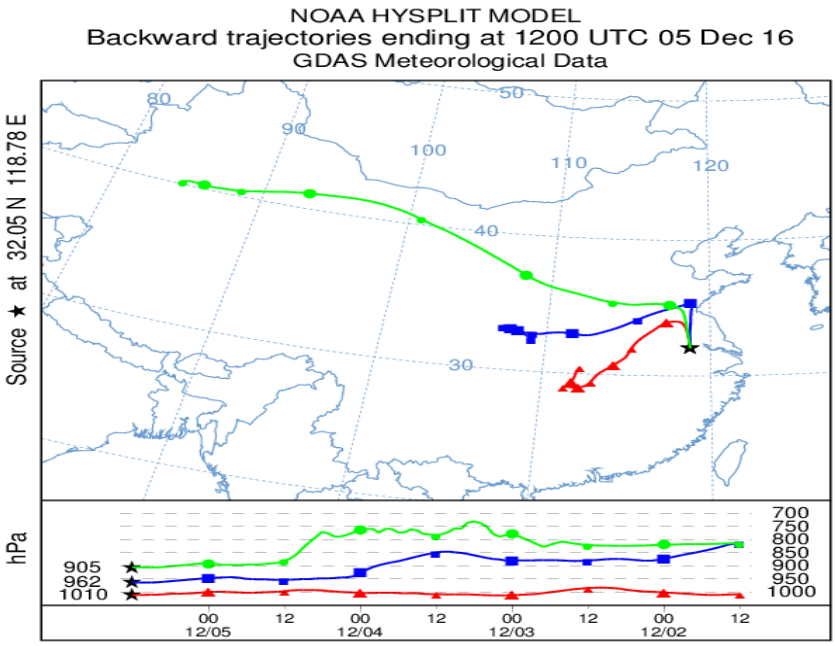

(f)

Fig 15. Time series during December 3-6, 2016, for (a) $PM_{2.5}$, BC and O_3 with associated meteorological parameters, trace gases and (b) optical parameters. Red markers represent O_3 over daily maximum average during winter. Weather charts on (c) 4th and (d) 5th December. (f) 96h backward trajectories analysis ending at 1200 UTC on 5th December.